energies

MDPI

Article

Bridging the Gap Between Earth Sciences and Mechanical Engineering: A Systematic Approach to Model Ground Source Heat Pumps with Deep Boreholes

Violaine Gascuel [1,2], Jasmin Raymond [1,*] and Christine Rivard [2]

[1] Institut National de la Recherche Scientifique, 490 Rue de la Couronne, Quebec City, QC G1K 9A9, Canada; violaine.gascuel@technorem.com
[2] Geological Survey of Canada, Natural Resources Canada, 490 Rue de la Couronne, Quebec City, QC G1K 9A9, Canada; christine.rivard@nrcan-rncan.gc.ca
* Correspondence: jasmin.raymond@inrs.ca

Abstract

Modelling of geothermal heat pump systems rarely integrates detailed surface and subsurface components. Simplifications such as neglecting the geothermal gradient, the different geological units intersected by the systems, and/or variable building loads, are common across current modeling approaches. These simplifications are particularly problematic for deep systems (e.g., >1 km). A new approach is presented to model a well doublet or a deep borehole heat exchanger (DBHE) with several heat pumps, which combines a comprehensive subsurface numerical model with codes capable of handling variable heat demand throughout the year. Groundwater flow and heat transfer are simulated with the subsurface model. Operating flow rates and number of activated heat pumps are adjusted during the simulation according to their efficiency and demand at a given time. Simulated heat production is constrained by technical and safety criteria to reflect realistic building conditions. The codes allow the simulation of cases in which the geothermal system is designed to partly meet demand, while maximizing its contribution. The thermal power production and electric consumption of the system are calculated. An illustrative example is provided for a sedimentary basin with a low geothermal gradient (~23.5 °C/km) using the Bécancour area in eastern Canada.

Keywords: geothermal; geo-exchange; well doublet; borehole heat exchanger; heat pump; building; dynamic simulation

Check for updates

Academic Editor: Ioan Sarbu

Received: 23 July 2026
Revised: 25 August 2026
Accepted: 28 August 2026
Published: 10 September 2026

Copyright: © 2026 by the authors. Licensee MDPI, Basel, Switzerland. This article is an open access article distributed under the terms and conditions of the Creative Commons Attribution (CC BY) license.

1. Introduction

Geothermal systems are increasingly recognized as an efficient way to heat and cool buildings using a reliable renewable energy source in low-temperature geological settings [1–4]. However, each site and project differ, both in terms of available geothermal resources and heating and cooling needs. Specific studies must therefore be conducted, typically including numerical models, to define sustainable operating parameters related to the subsurface (flow rate, injection temperature) prior to the development of a heating or cooling plant, allowing the design of a system that is adapted to the needs and resources [5].

Most existing deep systems (>500 m) for direct heat use are open loops (comprising pumping and injection wells) because they are efficient when a permeable aquifer is available at depth. Although less efficient, deep closed-loop systems (e.g., deep borehole

heat exchangers, DBHE) have gained in popularity in recent years, as they (1) can be installed in geological units that are not permeable, (2) are not subject to geochemical issues and (3) require less space than shallow closed-loop systems. Moreover, studies have suggested that closed-loop systems could be economically installed in abandoned oil and gas (O&G) wells (e.g., [6–8]).

A representative subsurface model is crucial when designing an open loop system. The sustainable flow rate and production temperature are controlled by the geological units' geometry, and hydrogeological and thermal properties, as well as the geothermal heat flux and surface temperature. The drawdown and drawup caused by a large open-loop system can affect an area extending over several kilometers. For these reasons, numerical models are often used at various stages in the development of an open-loop system to evaluate the geothermal potential of an area, to make informed decisions regarding its location (e.g., [9–11]), to design the geothermal wells [12,13], and to determine a sustainable operation scheme (e.g., [11,14,15]). However, these models are rarely coupled with heat pumps or used to model the heating or cooling operation of a specific building with a variable demand throughout the year.

The suitability of closed-loop systems is less dependent on the geological context (as they do not require permeable units) [13,16,17]. Nonetheless, the thermal conductivity and initial temperature of the subsurface have a significant impact on the system's efficiency [13]. The geothermal gradient and varying thermal properties across the geological succession result in variable heat transfer along the system length. Modeling studies of closed-loop systems coupled with heat pumps have generally focused either on the simulation of the energy use in a building or group of buildings or the simulation of the geothermal system itself [18]. Models detailing the subsurface generally simplify the demand, using a constant inlet temperature and flow rate (e.g., [13,19,20]) or a constant temperature difference between inlet and outlet and constant flow rate (e.g., [21,22]). These conditions are applied either during the whole simulation period, or at times when the system is operated (e.g., [20,23]). The actual heating and cooling demand for a building, however, fluctuates significantly throughout the year, even within the heating or cooling season.

The dynamic interaction between a building's heating or cooling load, a heat pump, and shallow borehole heat exchangers (BHEs) has been extensively studied, although most of these studies have considered a homogeneous subsurface (e.g., [24–26]). Some numerical models have, however, been developed to account for a stratified subsurface (e.g., [27–30]), natural groundwater flow (e.g., [27–29]), seasonal variations of the ground temperature (e.g., [27–29,31]) and/or the interactions between several BHEs (e.g., [29,31]).

The dynamic coupling of the heating or cooling demand and heat pumps with DBHEs has only been modeled in few studies (e.g., [32–35]). For example, Luo et al. [36] assessed the impact of the heat extraction distribution on the performance of a DBHE over the course of a heating season, without explicitly considering the heat pump, while Zhang [32] studied the impact of heat load distribution on a DBHE coupled with a single-stage heat pump. Both used synthetic heat extraction or heat demand scenarios, considering the same total heat extraction (or demand) distributed over time. A constant flow rate was used during DBHE operation, with a varying inlet temperature to fulfill the variable heat demand. The results demonstrate that scenarios with a higher peak load led to a lower rock temperature near the borehole and a lower outlet temperature at the end of the peak period compared to scenarios with a constant load during the heating season, resulting in lower *COP* values at these times [32]. Nonetheless, the simulations of Luo et al. [36] all showed the same ground and outlet temperature after heat recovery (outside the heating season). In Zhang [32], the

average *COP* for their different scenarios was similar to that obtained with a constant heat load (4.87–4.89 versus 4.91). However, when the time interval under intermittent operation was too long, or the peak heating load was too high, the fluid temperature at the DBHE inlet became very low, potentially compromising proper system operation. In such cases, they recommended the use of an auxiliary heating system. Furthermore, even in situations when the system is able to fulfill the peak demand, the lower *COP* during peaks implies a higher electric consumption. This highlights the importance of accounting for variable heating loads to obtain a representative simulation of a DBHE's operation, including its operating limits and optimum conditions. In addition, it is necessary to account for the total energy produced and consumed when optimizing ground heat exchangers coupled with heat pumps [37].

Recent studies by Thomasson and Abdurafikov [35], Wang et al. [33] and Wang et al. [34] have taken realistic building demands into account. Thomasson and Abdurafikov [35] and Wang et al. [33] considered relatively complex surface systems. The 2000 m DBHE investigated by Wang et al. [33] was connected either to a heat exchanger for direct heating or to a heat pump, depending on its simulated outlet temperature. In the study by Thomasson and Abdurafikov [35], the DBHE(s) (1 to 4 DBHEs with depths ranging from 800 m to 2400 m) are connected to two heat pumps in parallel through heat exchanger plates. The system also includes intermediate heat storage tanks on the consumer side. In both studies, the DBHE model was discretized vertically, allowing the geothermal gradient to be considered. However, uniform rock thermal properties were used (which may not be realistic given the depth of these systems). The surface ground temperature was also assumed to be constant. Furthermore, the DBHE model used in Thomasson and Abdurafikov [35] did not account for potential thermal interference in scenarios involving several DBHEs.

Wang et al. [34] considered a simpler surface system with a single heat pump connected to a 2000 m deep coaxial DBHE. The building heating load was used as an input. The DBHE and surrounding rocks were modeled numerically, with an added function to calculate a dynamic heat pump *COP* and the inlet temperature of the DBHE according to the heat demand and outlet temperature of the DBHE. The geothermal gradient and rock strata with different thermal properties were considered, as was the impact of seasonal temperature changes on the rock temperature in the shallow layers of the model.

Wang et al. [33], Wang et al. [34] and Zhang [32] each considered a constant operation flow rate for the DBHE throughout the simulation, varying the DBHE inlet temperature to fulfill the demand. However, shallow BHE studies have shown that reducing the flow rate would be more efficient under part-load conditions, as significantly less energy is required to circulate the fluid [38,39]. It stands to reason that the same would be true for DBHEs, in which pressure losses due to friction can be significant [6]. Furthermore, among these studies, only Thomasson and Abdurafikov [35] considered the possibility to use the DBHE(s) for both heating and cooling, and recognize that the DBHE(s) may not be able to always meet the full heating or cooling demand. Thomasson and Abdurafikov [35] are also the only ones to have included temperature-dependent properties for the heat carrier fluid, using a set of values of density, viscosity, specific heat capacity and thermal conductivity in heating mode, and another in cooling mode.

Only a few modeling studies have coupled heat pumps and detailed subsurface models of doublets in a dynamic manner. Baquedano et al. [40] studied a shallow groundwater heat pump system used for cooling, comprising a shallow doublet, a plate heat exchanger, and a single heat pump. The study assessed the impact of groundwater recycling (heated groundwater reaching the production well) on system efficiency. In Baquedano et al. [40], the thermodynamic model for the plate heat exchanger and heat

pump was built using the CoolPack modeling software, while the open loop geothermal system was modeled using FEFLOW. A plug-in was developed to couple these models and update the inlet temperature boundary condition at each time step. These coupled models were used to simulate continuous operation of the system for 180 days with constant cooling demand and flow rate. This model did not allow for variable inlet temperature or flow rate based on demand, nor did it consider the impact of groundwater temperature on its viscosity.

Some modeling studies focusing on standing column wells (another type of open-loop system) coupled with heat pumps have considered both detailed models for the subsurface and the heat pump system, as well as realistic building loads (e.g., [41,42]). Beaudry et al. [41] considered both a complex geology with different geological strata over 133 m having different thermal and hydraulic properties and hourly heating and cooling loads. The system studied included an auxiliary heater on the ground side, activated when the simulated temperature was too low, to prevent freezing. The operation of a system covering only part of the peak load (80%) could thus be considered, without simulating operation under temperature conditions in which the system would not be able to operate in the field. Several control strategies, including both constant and variable flow rates, were simulated. The variable flow rate strategy proved to be more effective. However, because the system was relatively shallow, the simulated groundwater properties were not modeled as temperature-dependent.

The main objective of the work presented in this paper was to develop codes that allow for the creation of an integrated tool that combines a detailed subsurface representation with heat pump operation for the design of two types of deep, low-temperature geothermal systems: geothermal doublets and DBHEs. These codes are novel as they integrate complex geology and variable energy demand, allowing the capacity of the geothermal systems, their energy consumption, and the need for auxiliary systems to be accurately assessed. Temperature-dependent properties are also considered for the groundwater in the doublet models.

The approach developed couples, as follows: (1) numerical models of geothermal systems designed in the FEFLOW 7.5 software, which integrate the subsurface geological features with their hydrogeological and thermal properties, as well as borehole components; and (2) Python 3.11.7 codes to calculate the heat production of the geothermal system, including the variable-efficiency heat pumps activated or deactivated according to the energy demand and the outlet temperature via interactive functions relying on variable building loads. Variable-speed heat pumps and water pumps are here considered, which allows the codes to adjust both the injection temperature and fluid flow rate according to energy demand and heat pump performance. In addition, the temperature range within which heat pumps can operate safely is accounted for by introducing entering source temperature thresholds below or above which heat pumps are automatically deactivated and bypassed.

Illustrative simulations were carried out with a realistic heating (and cooling) demand for a greenhouse considering the geological and hydrogeological context of the Bécancour area in the St. Lawrence Lowlands (eastern Canada), where the geothermal gradient is ~23.5 °C/km. As drilling costs are often an obstacle to the use of this low-carbon technology in such a context, re-purposed hydrocarbon wells are here modeled, but the method is just as applicable to newly drilled boreholes. A "conventional" approach to simulating the same study cases was also employed, using only the tools already available in FEFLOW for comparison.

2. Development of the Models and Codes

FEFLOW numerical models of doublets and DBHEs were developed, along with Python codes to simulate their operation and that of an above-ground heating system. The overall steps in this approach are as follows: (1) define the consumers' needs with building loads, (2) develop the numerical models for geothermal systems (doublets and/or DBHEs; Section 2.1), (3) choose the number and type of heat pumps and define a relationship between the entering source temperature and their performances (Section 2.2), (4) evaluate geothermal system capacities with preliminary simulations (Section 2.5), then (5) carry out dynamic simulations integrating the surface (heat pumps) and subsurface (doublet and DBHE) systems (Section 2.6), and finally compute the total energy production and energy consumption (Sections 2.3 and 2.4) all using the Python codes.

Four different codes have been developed: (1) to launch the simulation of a DBHE and record results, (2) to launch the simulation of a doublet and record results, (3) to make energy balances and graphs automatically for interpretation, and (4) to calculate the pressure losses. This article focuses mainly on the presentation and use of the launch codes, but all four are shared on GitHub (https://github.com/) (For details, please check Supplementary Materials).

The energy demand used to meet the needs of a given building (consumer) is not modeled as part of this method. The codes developed take monthly heating demand profiles as input parameters and assume that the heating and cooling demand will be the same each year. These profiles must be entered as lists with positive values for heating needs and negative values for cooling ones.

2.1. Characteristics of the Geothermal Systems Considered

The DBHE is assumed to be coaxial and used in both heating and cooling modes (Figure 1). Coaxial DBHEs have been recognized to be more efficient than other DBHE designs [43], and are used in most installed DBHEs [44–46]. In heating mode, the cold fluid reinjected in the DBHE would be injected in the annular space (i.e., annular inlet), while in cooling mode, the fluid would be injected into the central pipe (i.e., center inlet). By default, the DBHE system is considered to operate with two heat pumps, connected in series on the source side, but in parallel on the building side (Figure 1).

It was assumed that the doublet would be used for heating only, for a variety of reasons, including the issues associated with switching the flow direction (pumping or injection) in each well and the associated increased risks of chemical precipitation [47,48]. The bottom of both the production and injection wells was assumed to be an open hole. No skin effect (zone of modified permeability around a well) was considered in these simulations, and the doublet is by default considered to function with three heat pumps (Figure 1). However, to protect them from potentially corrosive brine, the loop feeding the source side of the heat pumps was separated from the geothermal brine by a plate heat exchanger forming an intermediate loop.

Both systems were designed to operate for at least 30 years.

Gascuel et al. [13] demonstrated that the temperature of the injected brine has a significant impact on the injection capacity of a doublet due to the evolution of density and viscosity with temperature. These properties were therefore modeled as temperature-dependent in the numerical model. In the illustrative example (Section 4), relationships predefined in FEFLOW were used (details in Gascuel et al. [13]).

To be compatible with the codes developed, 3D numerical models of the geothermal systems (DBHE or doublet) and surrounding subsurface built for a given project must meet the requirements listed in Table 1.

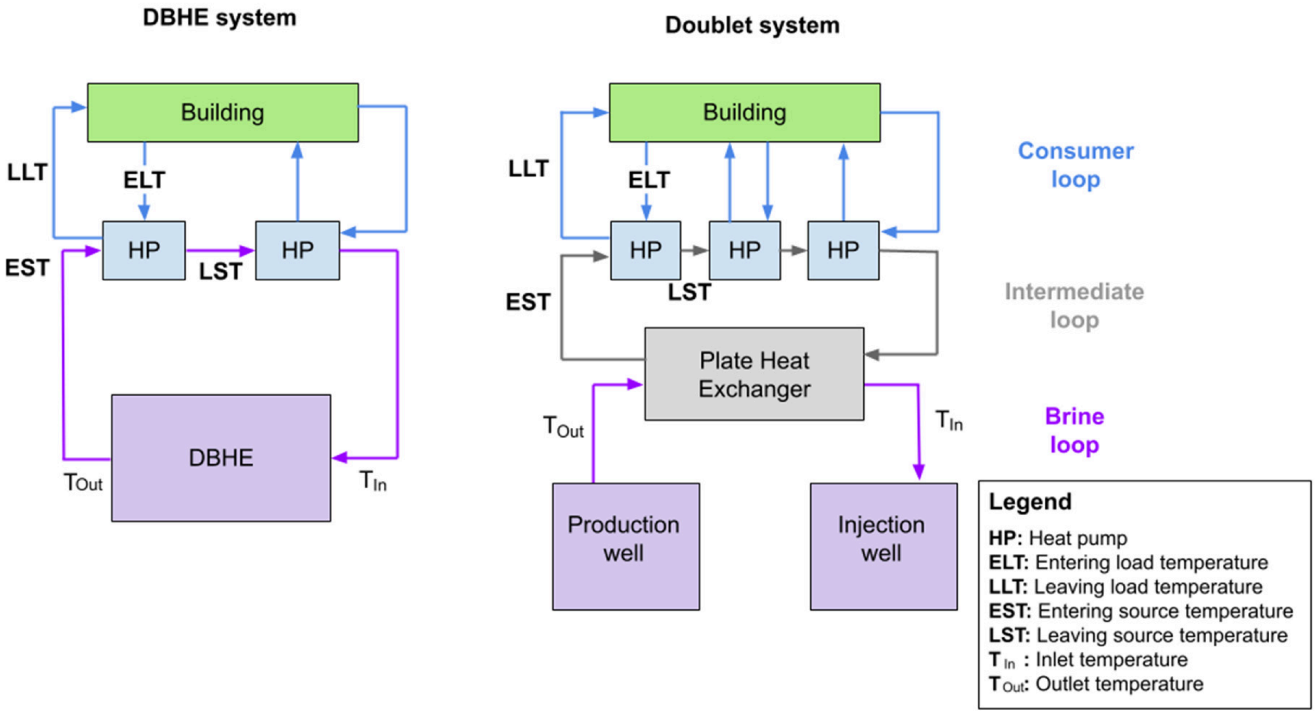

Figure 1. Schematization of the geothermal systems considered for simulation.

Table 1. Requirements of the numerical models.

Heat Transport	DBHE	Doublet
	Transient	**Transient**
Groundwater		
Flow	Steady state (if natural groundwater flow can be neglected)	Transient
Viscosity	Constant	Temperature-dependent
Representation of geothermal systems in FEFLOW	Use of the BHE tool with the analytical method of Eskilson and Claesson implemented in FEFLOW (see Diersch et al. (2011) [49])	Use of the multilayer well tool to represent the open sections of the wells, and define the diameter and the flow rate. Use of Dirichlet boundary condition on corresponding nodes to define the injection temperature. Other parts of the wells are not represented in the numerical model.

It is not possible to change the flow direction inside the DBHE in a FEFLOW model during a simulation. Thus, two models must be built for the DBHE, one with the injection taking place in the annular space (heating), and the other in the central pipe (cooling), with the same DBHE dimensions and subsurface characteristics. If a shutdown period for the DBHE is anticipated, a third model, identical to the others with the exception that it does not contain a BHE boundary condition, must also be prepared.

By default, FEFLOW assigns the number 0 to the first well created using the "multilayer well" tool, and the number 1 to the second. The Python code uses these numbers to call the wells, and assumes that Well 0 is the injection well and Well 1 is the production well. As FEFLOW also automatically assigns numbers to each node in a model, lists of the node

numbers corresponding to the injection well and production well must be made (those lists are used as an input in the code).

In the current code, wells forming the doublets are vertical. To allow for the use of deviated wells, it would be necessary to modify the function calculating temperature loss in the production well, as well as the function calculating pressure losses in both wells, as described in Gascuel et al. [13].

More specific information on the characteristics of the geothermal system models used in the illustrative example, including their design, mesh, boundary conditions and impact of temperature on the fluid parameters for the doublet, is provided in Section 4. These details could guide the development of such systems for another case study.

2.2. Heat Pump Models

A heat pump *COP* and its leaving source temperature (*LST*) depend on the entering source temperature (*EST*), the system's source flow rate, the temperature of the entering load fluid on the building side, the heat pump's load flow rate, as well as the heat pump itself. Heat pumps are more efficient (in terms of electricity consumption) when the temperature on the source side is higher for heating or cooler for cooling. Since the relationship observed using technical data for residential heat pumps is nearly linear, it was chosen to calculate the *COP* and *LST* of the heat pumps with a linear regression using their *EST* (Equations (1) and (2)). Parameters on the building side, such as entering load temperature or load flow rate, were fixed. Different linear regressions are used for different possible flow rates on the source side, as well as for heating and cooling modes. In our approach, the following relationships have been used:

$$COP = a_{\mathrm{COP}} \times EST + b_{\mathrm{COP}} \quad (1)$$

$$LST = a_{\mathrm{LST}} \times EST + b_{\mathrm{LST}} \quad (2)$$

Here, *COP* (-) is the coefficient of performance of a heat pump, *EST* (°C) the entering source temperature and *LST* the leaving source temperature. a_{COP}, b_{COP}, a_{LST} and b_{LST} are regression coefficients determined using performance data supplied by the manufacturer of the chosen heat pump for the given flow rate. In the illustrative example (Section 4), three different flow rates on the source side have been selected according to heat pump performance, yielding different pairs of coefficients for each flow rate in both heating and cooling modes (see Section 4.2).

The *EST* used in this calculation is either the outlet temperature of the DBHE for the first heat pump in the DBHE system, the temperature of the fluid leaving the plate-heat exchanger on the intermediate loop for the first heat pump in the doublet system, or the *LST* of the previous activated heat pump for subsequent heat pumps. In the pre-dimensioning estimates for the DBHE and doublet systems, the *EST* used was simply the simulated outlet temperature.

Thresholds have been implemented in the dynamic simulation code to prevent the activation of a heat pump if its *EST* is too low in winter or too high in summer for it to operate properly. The values of the minimum and maximum safe *EST* must be defined in the code according to the specifications of the chosen heat pump.

2.3. Computation of Heat Production

The numerical models simulate the outlet temperature of the system (or the temperature at the bottom of the production well for the doublet) but do not give direct access to heat production. Thus, heat production is calculated using a Python function, based on the simulated inlet and outlet temperatures over time and Equations (3)–(6). The cal-

culation is performed either after the simulation (for the pre-dimensioning preliminary phase, during which the suitability of the designed DBHE or doublet is assessed and the maximum flow rate to be used is determined, see Section 2.5) or during the simulation (for dynamic modeling).

For the pre-dimensioning of the system, the thermal power extracted from the geothermal system (DBHE or doublet) is calculated via (Equation (3)).

$$Power_{\mathrm{Geo}} = Q \times Cpv \times (T_{\mathrm{Out}} - T_{\mathrm{In}}) \quad (3)$$

where *Power* (W) is the power, *Cpv* (J m^{-3} K^{-1}) is the volumetric heat capacity of the fluid (either the heat carrier fluid in the DBHE or brine in the doublet), *T* (°C) is the temperature, Geo refers to the heat from the subsurface, Out refers to the fluid coming out of the ground, and In refers to the fluid reinjected in the ground.

Then, the total heat production provided to the consumer in heating mode (including the heat produced by the compressor of the heat pumps) is calculated with Equations (4) and (5).

$$Power_{\mathrm{Gen}} = Power_{\mathrm{Geo}} + Power_{\mathrm{Conso,HP}} \quad (4)$$

and

$$Power_{\mathrm{Conso,HP}} = Power_{\mathrm{Geo}} \times \frac{1}{COP - 1} \quad (5)$$

Here the subscripts Gen and Conso, HP refer to the power being generated by the system (or produced) and consumed by the heat pump, respectively.

In the preliminary evaluation, a global *COP* (-) is calculated for each simulation time step according to a linear regression on the *EST* (see Section 2.2), using T_{Out} as the *EST* and the maximum flow rate considered feasible on the source side with the chosen heat pump. This global *COP* is used to estimate the heat power generation and electric consumption of the heat pump(s) (which are not considered individually).

During the dynamic simulation, the calculation of the thermal power extracted and produced is performed individually for each heat pump, using the same Equations (3)–(5) but with the following three changes: (1) instead of T_{Out} and T_{In}, the *EST* and *LST* of the corresponding heat pump are used; (2) the *COP* of the heat pump is calculated with the regressions described in Section 2.2; and (3) the heat produced by each activated heat pump is summed to obtain the total heat production.

The Power produced is then integrated in an energy production over the course of the simulation (Equation (6)).

$$E_{\mathrm{Gen}} = \sum_{j=0}^{j=m-1} Power_{\mathrm{Gen}} \times (t_{j+1} - t_j) \quad (6)$$

where *E* (Wh) is the energy, *t* (h) is the simulation time, and *m* is the number of time steps at the end of the simulation.

2.4. Computation of Energy Consumption and Net Energy Production

The energy required to operate the systems at a given flow rate, and the corresponding net energy production, are essential for system design. In this method, they are calculated after the end of the simulations, in both the preliminary evaluation of the system capacity and in the interpretation codes for the dynamic simulation (detailed in GitHub).

The net energy production (E_{Net} in Wh) is defined as the energy (heat) produced by the system and provided to the consumer, minus the energy consumption of the system (Equation (7)).

$$E_{Net} = E_{Gen} - E_{\text{Conso,HP}} - E_{\text{Conso,Circu}} \tag{7}$$

The calculation of the energy consumption for the circulation system ($E_{\text{Conso,Circu}}$) is detailed in the Section 2.4.1. for the DBHE and Section 2.4.2 for the doublet, and the energy consumption of the heat pump system is detailed in Section 2.4.3.

2.4.1. DBHE Energy Consumption

The pressure loss by friction along the DBHE and the energy required to circulate the fluid are calculated using either the Blasius friction factor (Equation (8)), also used in Gascuel et al. [6], or the Haaland friction factor as presented by Nian et al. [8] (Equation (9)), depending on whether the user knows the roughness of the pipes and wants to take it into account or not [50]. Both are included in a Python function (modified version of the function in Gascuel et al. [6]; see the code on GitHub). These functions both consider the temperature dependence of the viscosity and density of the heat carrier fluid, using the temperature profiles in the annular space between the pipes and inside the inner pipe obtained from the FEFLOW simulation results. These functions are validated in the Appendix A.4.1. Additional tests have shown that the temperature profiles vary rapidly when the injection temperature and/or fluid flow rate change significantly. At present, the code is intended to simulate a monthly demand (assuming a constant demand within a month). Important changes generally occur in the first few days of the month because of important contrasts at the beginning and end of each month.

$$f_{\text{Blasius}} = \frac{0.3164}{{Re_{\text{i}}}^{0.25}} \tag{8}$$

$$\frac{1}{\sqrt{f_{Haaland}}} = -1.8 \times log_{10}\left[\left(\frac{\frac{\delta}{d}}{3.7}\right)^{1.11} + \frac{6.9}{Re}\right] \tag{9}$$

where f_{Blasius} (-) is the Blasius friction factor, f_{Haaland} (-) is the Haaland friction factor, Re is the Reynolds number, δ (m) is the roughness of the pipe and d (m) is the inside diameter of the pipe.

The pressure losses in the annulus and in the inner pipe are estimated with Equations (10) and (11), using the friction factor of either Blasius or Haaland.

$$\Delta P_{\text{In}} = \sum_i \frac{f_{\text{Annulus}} \times {v_{\text{Annulus}}}^2}{2 \times g \times \left(r^i_{\text{Outer}} - r^o_{\text{Inner}}\right)} \tag{10}$$

$$\Delta P_{\text{Out}} = \sum_i \frac{f_{\text{Inner,i}} \times {v_{\text{Inner}}}^2}{4 \times g \times r^i_{\text{Inner}}} \tag{11}$$

The last pressure loss term to be considered is related to both the sudden change in fluid flow direction at the bottom of the DBHE and the abrupt change in the pipe section (S) (between the annulus and the inner space). This additional pressure loss is called $\Delta P_{\text{Singularity}}$. This specific pressure loss has been considered using the empirical correlations in Equations (12)–(15), also used in Gascuel et al. [6].

$$\Delta P_{\text{Singularity}} = \frac{\left(Coef_{\text{Bend}} + Coef_{\text{Section}}\right) \times {v_{\text{Inner}}}^2 \times \rho_{\text{Bottom}}}{2} \tag{12}$$

$$Coef_{\text{Bend}} = 1.3 \times (1 - \cos(\beta)) \tag{13}$$

Here, β refers to the angle of the bend.

In the case of DBHEs, this angle is always equal to the number π (rad) as the fluid flow makes a U-turn. The coefficient used to calculate the pressure loss due to the change in flow section ($Coef_{\text{Bend}}$) is calculated with Equation (10).

$$Coef_{\text{Section}} = \left(\frac{1}{c} - 1\right)^2 \tag{14}$$

where

$$c = 0.59 + 0.41 \times \left(\frac{S_{\text{Inner}}}{S_{\text{Annulus}}}\right)^3 \tag{15}$$

Finally, the total pressure loss due to the fluid circulation is calculated with Equation (16), corresponding to the sum of the losses calculated previously using Equations (10)–(12).

$$\Delta P = \Delta P_{\text{In}} + \Delta P_{\text{Out}} + \Delta P_{\text{Singularity}} \tag{16}$$

There is only a slight difference in temperature inside the DBHE from one year to the next (at the same time of the year). However, for a temperature variation to impact energy losses by friction, the variation must be significant. It was therefore deemed acceptable to use just one temperature profile per month for all simulated years. The temperature profiles corresponding to the temperature inside the DBHE on the 10th day of each month (i.e., once the temperature has stabilized), computed for the first year of simulation, were used. The power required to circulate the fluid is here calculated at each time step (same timesteps as in the FEFLOW simulations), accounting for the variation in fluid flow rate (Equation (17)). In the model, a circulation pump efficiency of 85% was assumed. These power values were then used to calculate the energy required to circulate the fluid during the simulation period (Equation (18)).

$$Power_{\text{Conso,Circu}} = \frac{Q \times \Delta P}{\eta} \tag{17}$$

$$E_{\text{Conso,Circu}} = \sum_{j=0}^{j=m-1} P_{\text{Conso,Circu}} \times (t_{j+1} - t_j) \tag{18}$$

where ΔP (Pa) is the pressure loss due to friction, η (-) is the efficiency of the circulation pump, and Conso,Circu refers to the electricity consumption of the circulation pump.

2.4.2. Doublet Energy Consumption

Energy consumption for the doublet pumps (for brine pumping and injecting) is calculated using a Python function (presented in Gascuel et al. [13] and available on GitHub) and considers energy losses due to friction in the wells. The simulated temperature at the bottom of the production well is used to calculate the energy loss by friction in this well. The simulated injection temperature at each time step is used to calculate the energy loss by friction in the injection well. The power requirement for both wells is calculated in the same manner as for the DBHE, assuming again a pump efficiency of 85%. The energy required to circulate the heat carrier fluid in the plate heat exchanger has been neglected. The validation of functions developed to calculate pressure loss in the doublet is presented in Appendix A.4.2.

2.4.3. Energy Consumption of the Heat Pumps

The power consumption of the heat pumps is determined using Equation (5). It is then integrated over the course of the simulation to obtain the energy consumed by the heat pumps (Equation (19)).

$$E_{\text{Conso,HP}} = \sum_{j=0}^{j=m-1} Power_{\text{Conso,HP}} \times (t_{j+1} - t_j) \quad (19)$$

The energy required to circulate the heat carrier fluid from a heat pump to another was neglected.

2.5. Preliminary Evaluation of Maximum Fluid Flow Rates and the Heating and Cooling Capacities of Systems

The capacity of the geothermal systems and the maximum flow rate that should be used when operating at full capacity are considered unknown prior to the first simulations. Preliminary simulations must therefore be carried out to provide initial estimates since dynamic simulations can require long computation times. It is deemed worthwhile to run preliminary simulations with simpler operation parameters over a complete heating or cooling season. These provide a first estimate of the maximum capacity of the designed system, which could be used to adjust the systems to better match the demand before going further. The maximum flow rate for systems when operating at full capacity for long periods is also estimated, knowing that an auxiliary system would likely be required to handle peak demand for heating or cooling.

2.5.1. DBHE System

The amount of heat the DBHE can produce is proportional to the difference between its inlet and outlet temperatures. Even though the inlet and outlet temperatures are strongly correlated [51], a lower inlet temperature in the DBHE (or *LST* of the heat pump) leads to a greater temperature difference with the surrounding rock and thus a greater heat production. Heat extraction or injection from the DBHE system is therefore respectively limited by the minimum or maximum *LST* achievable by the last heat pump activated, which in turn is limited by the minimum or maximum *EST* acceptable for its safe operation (by default −6.7 °C or 43.3 °C in the model, see Section 4.2). To evaluate the maximum heating capacity of the system, the *LST* corresponding to the minimum *EST* acceptable for safe operation of the chosen heat pump model is calculated for the maximum source flow rate at which the heat pump can operate.

Numerical simulations using this minimum *LST* as the inlet temperature for the DBHE are run using different constant flow rates for the duration of the heating season. The corresponding thermal power production, electricity consumption of the circulation pump, and electric consumption of the heat pump are calculated using the linear regressions presented in Section 2.2 and equations presented in Sections 2.3 and 2.4. The optimum fluid flow rate (maximizing the net energy production of the DBHE) and the system capacities (i.e., assumed to correspond to the thermal power produced in these preliminary simulations) can then be estimated. It would not be worthwhile to use a greater flow rate, even at times when demand exceeds what can be produced at this flow rate, as the extra electricity required to operate the DBHE at a higher flow rate would be used more efficiently in an electric radiator. The flow rate used in the dynamic simulations should thus never be greater than this flow rate.

Calculating the electricity consumption of the heat pump and circulation pump also allows the definition of heating demand thresholds below which it is not beneficial to use the DBHE and heat pump systems, hence when the use of the auxiliary electrical system should be preferred. The same calculation is performed to assess the cooling capacity of

the DBHE system and maximum flow rate in cooling mode. However, in cooling mode, the following pertains: (1) the *LST* corresponding to the maximum safe *EST* is used as the inlet temperature, (2) the DBHE is modeled with the central pipe as the inlet (i.e., the returning fluid ascends through the annular space), (3) the simulations are run for the duration of the cooling season, and (4) the linear regressions for the cooling *COP* of the heat pump are used instead of heating *COP*s.

2.5.2. Doublet System

It is unlikely that a doublet will be used with an inlet temperature corresponding to the minimum *LST* achievable by the heat pump. Due to imperfect heat transfer in the plate heat exchanger, the temperature of the injected brine is inevitably higher than the outlet temperature of the last activated heat pump. Furthermore, the freezing point of the reinjected groundwater (or brine) or geochemical reactions may dictate a lower limit to the injection temperature. An injection temperature close to the mean expected injection temperature in winter was thus used here for the preliminary evaluation of the doublet performance (10 °C is used in the example in Section 4, as it seemed to be a reasonable value based on doublets currently in operation with heat pumps under relatively similar conditions, such as those in Plessis-Robinson, France).

The limiting factor for the doublet operation is the safe fluid flow rate for brine extraction and injection, established considering the injection pump capacities and to prevent induced seismicity. By default, a hydraulic head threshold of 500 m at the injection well, corresponding to an overpressure of ~5 MPa, was chosen for the simulation period, as in Gascuel et al. [13], based on the work of Korzani et al. [52]. As the periods during which the doublet would not be in operation are assumed not to be long enough for the hydraulic heads to return to equilibrium, long-term simulations are required to define the maximum safe flow rate.

Preliminary simulations of the doublet are run for scenarios with constant flow rates during the heating season (for instance, 2, 3 or 4 L s^{-1}, from October to April included, are used in the example in Section 4), with no doublet operation during the rest of the year. To speed up the preliminary simulations over 30 years, an equivalent constant annual flow rate has been calculated and applied to the first 29 years of simulation (Equation (20)), while the variable flow rate pattern is applied only during the heating season in the 30th year. The maximum safe flow rate can then be determined using a linear regression on the maximum injection head recorded in each of these simulations (which is reached at the end of the 30th year heating season),

$$Q_{\text{eq}} = Q \times \frac{t_{\text{heating season}}}{365.25} \tag{20}$$

where Q (L·s^{-1}) is the flow rate applied during the heating season and $t_{\text{heating season}}$ (d) is the duration of the heating season. The maximum drawdown simulated at the production well with this flow rate must not drop below the top of the reservoir. If it does, this condition becomes the limiting factor, and a linear regression of the maximum drawdown versus flow rate must be used to define the maximum flow rate instead.

2.6. Dynamic Simulations

The principles used in the codes are described in the subsections below. The main goal of these codes is to determine the inlet temperature and the flow rate that should be used by the geothermal system at each time step (Pre-time step function), adapting their heat or cold production to both the heat consumer needs and the capacities of the heat pumps. These values are then assigned to the numerical model as boundary conditions.

For the DBHE, two different scenarios are used: Code 1—with two heat pumps available for heating and one for cooling, and Code 2—with two heat pumps available for both heating and cooling. However, the benefit of using a second heat pump for cooling is expected to be limited, given that the temperature at depth is relatively high. For the doublet, only one scenario is used (called "Code"), where three heat pumps are used for heating (as no cooling is considered).

2.6.1. Temperature at the Geothermal System Outlet

The first steps in the Pre-time-step functions for both the DBHE and doublet serve to determine the time of the year (month when using monthly energy demands) in the simulation, and to access the outlet temperature of the DBHE or doublet calculated by the numerical model. The DBHE numerical model in FEFLOW already simulates heat transfer to and from the fluid while it rises to the surface. Thus, the modeled outlet temperature can be used directly by the control function as the *EST* of the first heat pump.

Only the well screens or open portions are simulated in the doublet numerical model. However, as the production well crosses geological units that are cooler than the reservoir, the ascending brine in a doublet is cooled by conduction as it rises [53]. It is therefore necessary to calculate this heat loss in the production well in the code. The Python code retrieves the brine temperature at the bottom of the open part of the well simulated by the numerical model. Then, another Python function, modified from the code GEOPHIRES V2.0 [54] and described in Gascuel et al. [13], was used to calculate the heat losses in the production well based on the method of Ramey [55]. This method considers the fluid flow rate, operating time, as well as the average thermal properties of the rocks crossed by the well. However, the thermal resistance of the casing and cement is neglected, and direct conductive heat transfer between the brine and the surrounding rock is considered. It was verified in Gascuel et al. [13] that this simplification has a negligible effect. Since this paper focused on a relatively shallow well (900 m deep with a diameter of 203 mm), a further validation of this function was performed in this paper using the results of Brown and Falcone [56] for a 2000 m-deep production well with a similar diameter (216 mm) (Appendix A.2).

The function used to calculate heat loss in the production well was slightly modified compared to the one used in Gascuel et al. [13]. At each time step during the heating season, a utilization factor was calculated using Equation (21) to account for previous variations of the flow rate and applied to the temperature loss. This utilization factor (*Utilfactor*) is here assigned a value of 1 at the beginning of each heating season, assuming the rocks surrounding the well have time to cool down to their ambient temperature during the summer. This approach is also used in GEOPHIRES V2.0, although a single utilization factor calculated for the lifetime of the doublet is used [54].

$$Utilfactor = \frac{\sum_{j=s}^{j=n-1} Q_{B,j} \times (t_j - t_{j-1})}{\sum_{j=s}^{j=n-1} Q_{B,n-1} \times (t_j - t_{j-1})} \quad (21)$$

where Q_B ($m^3 s^{-1}$) is the brine flow rate, t (s) is the simulation time, n (-) is the number of time steps since the beginning of the heating season and s is the time step corresponding to the start of the current heating season.

It was numerically verified in Gascuel et al. [13] that accounting for heating by conduction of the injected brine while flowing into the injection well had no significant impact on the hydraulic head of this well or on other parameters relevant to the performance of

a doublet. Conduction in the injection well was therefore not considered for doublets in this study.

2.6.2. Control of Heat Pumps

Python functions have also been developed to simulate the operation of the surface system, enabling the determination of when and at what fluid flow rate one or more heat pumps should be activated. The operating principle of these functions is shown on Figure 2. At each time step, these functions use the outlet temperature of the DBHE (FEFLOW output) at the previous time step to calculate the *COP*, *LST* and heat production of each heat pump, if activated. Then, every 4 h of simulated time, the code decides whether each heat pump should be activated. It also determines the fluid flow rate to be applied to the geothermal system according to the demand and the constraints imposed. Conditions have been added to these functions to avoid using heat pumps with an *EST* that could compromise their operation (see Section 2.2). Based on this decision, the code then calculates the inlet temperature to be applied to the DBHE or temperature of the fluid in the intermediate loop entering the plate heat exchanger for the doublet. This inlet temperature is used as input for the next time-step of the FELFOW model to ensure dynamic simulations.

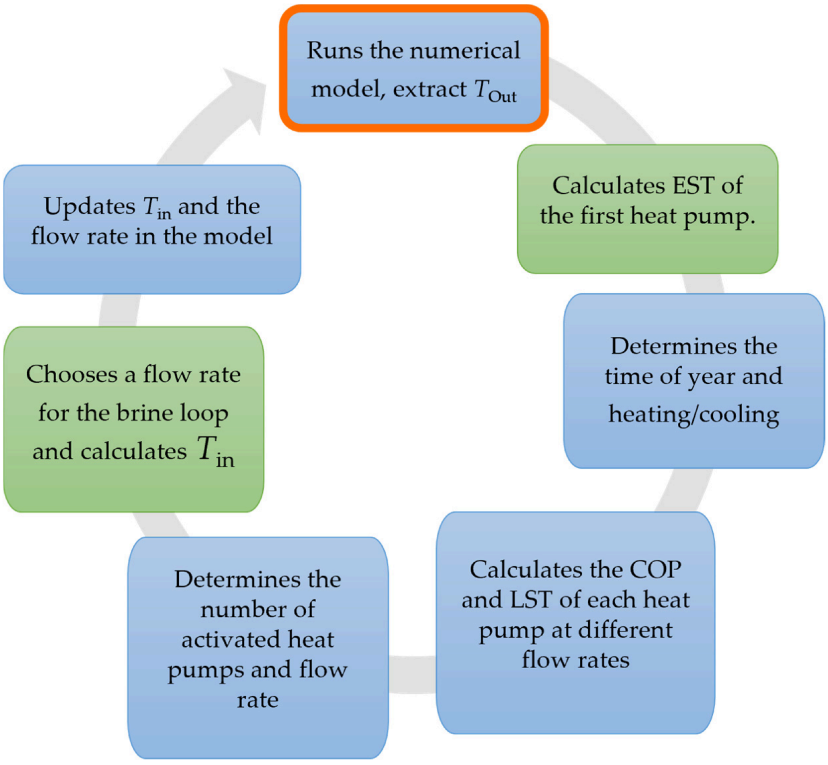

Figure 2. Principle of the core function controlling the activation of heat pumps and flow rate(s). The step outlined in orange is done with FEFLOW, while the others are performed with Python codes. The steps in blue apply to both the DBHE and doublet simulations, while the steps in green only apply to the doublet simulation. Note that for the DBHE, the T_{Out} from the model can be used directly as the *EST* of the first heat pump, and the T_{in} is the *LST* of the last activated heat pump.

The total thermal power produced (i.e., the sum of the thermal power supplied by each activated heat pump) is calculated by the code and recorded at each time step with Equation (4). Indeed, the heating or cooling capacity of the system is limited by the number of heat pumps and by their minimum or maximum *EST* thresholds, implying that the heating or cooling demand may not always be fulfilled.

Another condition has been added to prevent over-production and energy waste, namely, heat demand must exceed heat production by at least 10% with a certain flow rate and number of activated heat pumps before activating additional heat pumps or increasing the flow rate passing through the heat pumps. This percentage is arbitrary and could easily be modified. It was set to avoid overproduction, as if, for example, the increase in demand were less than 10% of current production, activating an additional pump would result in significant overproduction. The same condition was applied in cooling mode for the DBHE.

Finally, the entire geothermal system with heat pumps is shut down if the heating or cooling demand is considered too low to justify operating the system with the minimum flow rate and one heat pump (in other words, operating it would consume more energy than using a regular electric heater).

2.6.3. Fluid Heat Capacity

The *EST* of the heat pumps can change significantly throughout the year, leading to non-negligible variations in the heat capacity of the heat carrier fluid. Thus, another Python function has been used to calculate the heat capacity of the fluid entering each heat pump at each time step, to ensure that the calculated heat pump production is as realistic as possible. An interpolation of the data tabulated in Chapter 21 of the ASHRAE Handbook for 30% propylene glycol was used [57] for the DBHE as well as in the intermediate loop of the doublet system (using a function developed by Pr. Louis Lamarche of ÉTS; personal communication). As the tables do not provide heat capacity values for temperatures below −5 °C, the value corresponding to −5 °C was used when the fluid temperature was lower.

The production temperature and *EST* of the heat pumps vary less for the doublet than for the DBHE. It was thus deemed acceptable to use a single heat capacity value for both the brine produced and the fluid in the intermediate loop in the doublet (see Figure 1). The brine heat capacity assigned in the model is based on the initial average temperature of the reservoir at the production well location and other properties, according to the empirical equations of Jamieson et al. [58] reported in Nayar et al. [59] (Equations (22)–(26)). The function used to calculate the brine heat capacity was validated for NaCl solutions (Appendix A.1). The fluid in the intermediate loop was a mix of propylene glycol (an antifreeze) and water. Its heat capacity can be calculated using the same interpolation as for the DBHE.

$$Cpm_B = A + B \times (T_{\text{Ref}} + 273.15) + C \times (T_{\text{Ref}} + 273.15)^2 + D \times (T_{\text{Ref}} + 273.15)^3 \quad (22)$$

A, B, C and D are coefficients defined as follows:

$$A = 5.328 - 9.76 \times 10^{-2} \times \frac{1000 \times TDS}{\rho_B} + 4.04 \times 10^{-4} \times \left(\frac{1000 \times TDS}{\rho_B}\right)^2 \quad (23)$$

$$B = -6.913 \times 10^{-3} + 7.351 \times 10^{-4} \times \frac{1000 \times TDS}{\rho_B} - 3.15 \times 10^{-6} \times \left(\frac{1000 \times TDS}{\rho_B}\right)^2 \quad (24)$$

$$C = 9.6 \times 10^{-6} - 1.927 \times 10^{-6} \times \frac{1000 \times TDS}{\rho_B} + 8.23 \times 10^{-9} \times \left(\frac{1000 \times TDS}{\rho_B}\right)^2 \quad (25)$$

$$D = 2.5 \times 10^{-9} + 1.666 \times 10^{-9} \times \frac{1000 \times TDS}{\rho_B} - 7.125 \times 10^{-12} \times \left(\frac{1000 \times TDS}{\rho_B}\right)^2 \quad (26)$$

Here, Cpm (J $K^{-1}kg^{-1}$) is the specific heat capacity, T_{Ref} (°C) is the reference temperature (here 31 °C), ρ (kg m^{-3}) is the volumetric mass density, TDS (g kg^{-1}) is the total dissolved solids content of the brine, and B refers to the brine.

2.6.4. Additional Considerations for the Doublet System

Change in Brine Density Between the Production and Injection Wells

The density of the brine increases as it cools in the plate heat exchanger. Thus, to maintain the same mass flow rate, the fluid flow rate in the injection well must be slightly lower than in the production well. The injection flow rate is hence recalculated each time the production flow rate of the doublet changes, based on the production flow rate selected and the temperature of the brine injected. The flow rate changes in the dynamic simulation correspond to significant changes in the demand or temperature of the produced brine. Thus, times when the flow rate changes also correspond to times when the change in injection temperature is the greatest. The method presented in Gascuel et al. [13] was used.

Plate Heat Exchanger

The heat transfer efficiency (eff) of the plate heat exchanger is assumed to be 90%, as in Gascuel et al. [13]. According to Brown et al. [60], this percentage could realistically be achieved. The code was written in a way that allows the fluid in the intermediate loop to be either freshwater, or a mix of water and propylene glycol, with a proportion of propylene glycol chosen by the user. In the illustrative example, because preliminary runs showed that the temperature in this loop never decreased below 0 °C, freshwater was chosen as the circulating fluid in the intermediate loop (Figure 1). A Python function has been developed to calculate the injection temperature assigned to the doublet (T_{in}) and the EST of the first activated heat pump at each time step, based on the fluid flow rates in the intermediate and building loops and the LST of the last activated heat pump. It was validated in Appendix A.3 by reproducing results from Brown et al. [60].

The function first calculates the maximum amount of heat that could be transferred ($\check{Q}_{max}$) if the heat transfer efficiency were 100% (Equation (27)).

$$\check{Q}_{max} = \min(Q_B \times Cpv_B, Q_w \times Cpv_w) \times (T_{Out} - LST_{last\ HP}) \quad (27)$$

where $\check{Q}$ (Wth) is the heat transfer through the plate heat exchanger, min is the minimum function, and w refers to the mix of water and antifreeze circulating in the intermediate loop. Then $\check{Q}_B$, the effective amount that would be transferred, is calculated (Equation (28)), as

$$\check{Q}_B = eff \times \check{Q}_{max} \quad (28)$$

where eff = 90%.

This heat transfer is then used to calculate the fluid temperature exiting the plate heat exchanger on each side via Equations (29) and (30).

$$T_{In} = T_{Out} - \frac{\check{Q}_B}{Q_B \times Cpv_B} \quad (29)$$

$$EST_{first\ HP} = LST_{last\ HP} + \frac{\check{Q}_B}{Q_w \times Cpv_w} \quad (30)$$

Control of the Fluid Flow Rate in the Brine Loop

The function also controls the flow rate in the intermediate loop. However, as the intermediate loop and brine loop are separated by a plate heat exchanger (Figure 1), they

can operate at different flow rates. Varying the flow rate in the brine loop can help adjust the heat production, decreasing it to decrease the pumping energy consumption at times when the heat demand is lower, and increasing it to meet the heat demand while keeping a high heat pump *COP* when the demand is higher.

It was therefore necessary to define under which conditions the production flow rate would be increased or decreased, and what the minimum and maximum allowed flow rates would be. As heat pumps operating with a low *COP* consume more electricity, it was decided to use both the fulfillment of the heat demand and the value of the mean *COP* for the activated heat pumps as criteria to either increase or decrease the fluid flow rate. A minimum flow rate (by default 1.5 L s^{-1}) was set in the pre-time step function. This minimum flow rate was selected to avoid significant cooling of the brine in the production well. This minimum value is the default value at the beginning of the heating season (prior to the execution of the pre-time step function). The production flow rate is increased if either the system produces less heat than the heat demand, or the average *COP* of the active heat pumps is below 3.5. This value is considered reasonable given the efficiency of geothermal heat pumps, and can be changed if needed. The new flow rate is set to the lower value between 110% of the previous flow rate and the maximum allowed flow rate defined by the user. The value of 110% allows for a progressive increase in the flow rate, suited to finding the most appropriate flow rate and also for the numerical stability of the simulation. If the heat production of the system is greater than 110% of the heat demand and the average *COP* of the activated heat pumps is greater than 3.6, the production flow rate is reduced. It is either decreased by 10% or set to the minimum flow rate defined by the user, depending on which is the highest.

The inlet temperature is then calculated by the plate-heat exchanger function considering this new flow rate and the conditions on the intermediate loop side. As there is a lower limit on the injection temperature in the doublet (the brine could freeze), a security injection temperature threshold was fixed. Thus, if the calculated injection temperature at this stage is lower than the minimum injection temperature set by the user, the injection temperature is set to this minimum injection temperature, and the production flow rate is recalculated. If the recalculated flow rate is greater than the maximum, the maximum flow rate is used. In that case, the heat demand may not be entirely met.

2.6.5. Control of Time Step Duration

The automated time-step control in FEFLOW software was used. A second-order accurate predictor corrector scheme with a maximum Euclidian L2 error tolerance of 10^{-3} (dimensionless) was selected in the numerical models. Additionally, each time the simulations are relaunched, the initial time step has a fixed maximum duration of 0.001 days. The growth factor between subsequent time steps was restricted to a maximum of 1.2.

In the DBHE simulation, the code restarts the simulation at the beginning of each month, ensuring small time steps at the beginning of the month when the changes in heating and cooling demand, and thus in operating conditions, are most important. The code also allows for changing models between the heating and cooling periods when the flow needs to be reversed (see Section 2.1). The temperature in the model is then updated before the start of the simulation for the new month using the temperature matrix at the end of the simulation of the previous month in the other model. The maximum length of a time step was fixed to 10 days.

For the doublet, a new simulation is relaunched every time the flow rate in the doublet is changed. The temperature and hydraulic head assigned to every node in the

numerical model are updated before the beginning of each simulation, using the values simulated at the end of the previous simulation. In this way, every time the flow rate changes, the time steps become small again. Furthermore, whenever the change in inlet temperature relative to the previous time step is greater than 0.1 °C, the code sets the maximum time step size to 0.001 day. In all other cases, the maximum time step size is set to 1 day.

3. Comparison with a Conventional Approach

The results of dynamic simulations of the systems obtained using the developed codes were compared to those obtained using a "conventional approach," using the same example to assess the gains in outlet temperature, *COP* or system performance. This approach, focusing on the subsurface model, uses only tools available in the FEFLOW interface. A common method of simulating varying operating conditions over time using software such as FEFLOW is to impose pre-defined time series as boundary conditions. To compare the results obtained from both types of simulations, the models were run for a year to simulate heat extraction and injection in the DBHE and inlet temperature or flow rate in the doublet, using the Python codes (dynamic) and without using them (conventional).

Two scenarios of boundary conditions were chosen for the DBHE. Both are predefined heat extraction time series (one of the boundary conditions available in FEFLOW's BHE interface). In the Time series 1 scenario, it was assumed that modelers do not have prior knowledge of the heating or cooling capacities of the geothermal system they are modeling. The boundary condition controlling heat production is thus calculated directly from the heating/cooling demand using a constant value for the heat pump *COP* (one value for the heating and one value for the cooling mode). This assumption implies that the heat extraction and injection rates may be unrealistic. In Time series 2, it is assumed that the modelers have already run a preliminary simulation and thus know if the DBHE can or cannot fulfill the entire heating and cooling demand. If it is unable to, the heat extraction and injection imposed in the model are therefore limited according to the system capacity at the end of the corresponding month in the preliminary simulation with the optimal fluid flow rate. For comparison purposes, both time series were created using the average heat pump *COP* from the dynamic simulation results for the heating and cooling seasons, respectively. The flow rate used is constant in these simulations. To achieve the imposed heat extraction or injection, FEFLOW uses a new inlet temperature at each time step, calculated from the outlet temperature simulated at the previous time step, the flow rate, and the heat capacity of the heat carrier fluid.

The doublet was simulated using a pre-defined flow rate time series applied to the production and injection wells, which is a common approach (e.g., [48,61,62]). To define these time series, the production temperature was assumed to be constant and equal to the initial reservoir temperature near the open section of the production well. In the same manner as for Time series 1 and 2 for the DBHE, the average heat pump *COP* obtained from the dynamic simulation using the developed code was used to determine the flow rates corresponding to the heat demand.

Three approaches have been used to interpret and compare energy production (Table 2). Firstly, the results can be interpreted simplistically, assuming that the temperature simulated at the bottom of the production well by FEFLOW is the temperature at the well outlet (thus neglecting heat losses by conduction) and using a constant *COP* for the heat pumps (the same that was used to define the time series). This method is called "R" (for "raw"). Secondly, a variable *COP* can be considered, being a function of the temperature simulated in the production well by FEFLOW, neglecting heat losses in the

production well (called "TCOP" for "temperature dependent *COP*"). The third approach involves recalculating the outlet temperature of the production well, considering heat losses and using a variable *COP* calculated using this recalculated temperature (called "HL" for "heat losses").

Table 2. Phenomena considered when interpreting the results of the conventional simulations.

Name of the Results	Phenomena Considered	
	A *COP* Re-Calculated Using the Simulated Outlet Temperature of the Production Well	**Heat Losses by Conduction in the Production Well (Doublet Only)**
R (for «raw»)	✗ (fixed *COP*)	✗
TCOP (for temperature dependant *COP*)	✓	✗
HL (for heat losses)	✓	✓

4. Illustrative Example Using Abandoned Wells in the Bécancour Area (Eastern Canada) to Heat a Greenhouse

4.1. Heat Consumer

Given that greenhouses are major consumers of heating energy and that food autonomy is increasingly sought, a 4000 m^2 bell pepper greenhouse was used as an example of a consumer, with the heating and cooling demand defined by Semple et al. [63] for the climate of Montréal (located 177 km from Bécancour) for a closed greenhouse (i.e., without natural ventilation in order to reduce water consumption and the risks of pests). Only monthly demand was provided. Thus, it was considered that demand in the model did not vary within a month (Figure 3). In this example, the heating season starts in October and lasts 212 days, while the cooling season starts in May and lasts 153 days. The decrease in energy demand in December is due to agricultural practices. The crops are terminated in late November, and replanted in early January.

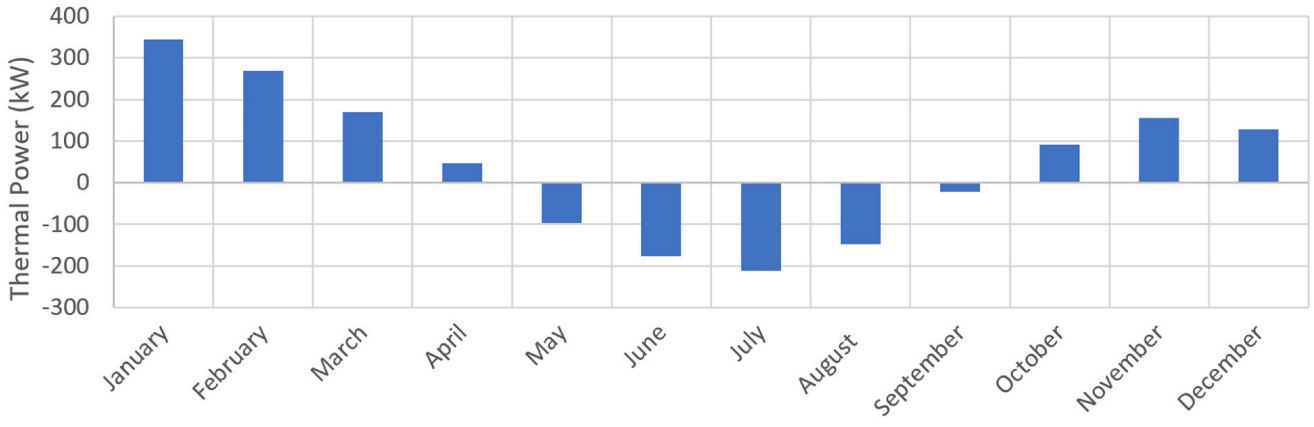

Figure 3. Heating and cooling loads used for the greenhouse in the example. The positive power requirement corresponds to heating loads, and negative ones to cooling loads.

4.2. Heat Pumps

The performance and *LST* of heat pumps depend on the entering temperature and flow rates on both sides. Since the model focuses on the geothermal side, assumptions were made regarding the temperature and flow rates on the building side (Table 3). The specifications of the HT180-Geosmart heat pumps [64] are here used as illustra-

tive examples. This heat pump is capable of operating with source fluid flow rates between 1.51 and 3.03 L s^{-1}, allowing flow rate adjustment under part load conditions. In these examples, only discrete flow rates of 1.5, 2.3 and 3.0 L s^{-1} are considered possible, corresponding to 24, 36 and 48 gpm, which are the tabulated test flow rates in the heat pump's performance table provided by the supplier. Interpolations of the *COP* and *LST* depending on *EST* are displayed on Figures 4 and 5, based on Equations (1) and (2). Furthermore, minimum and maximum *EST* thresholds of −6.7 °C and 43.3 °C were defined for the heating and cooling modes, respectively, based on the minimum and maximum tabulated values for the maximum source flow rate (3.0 L s^{-1}).

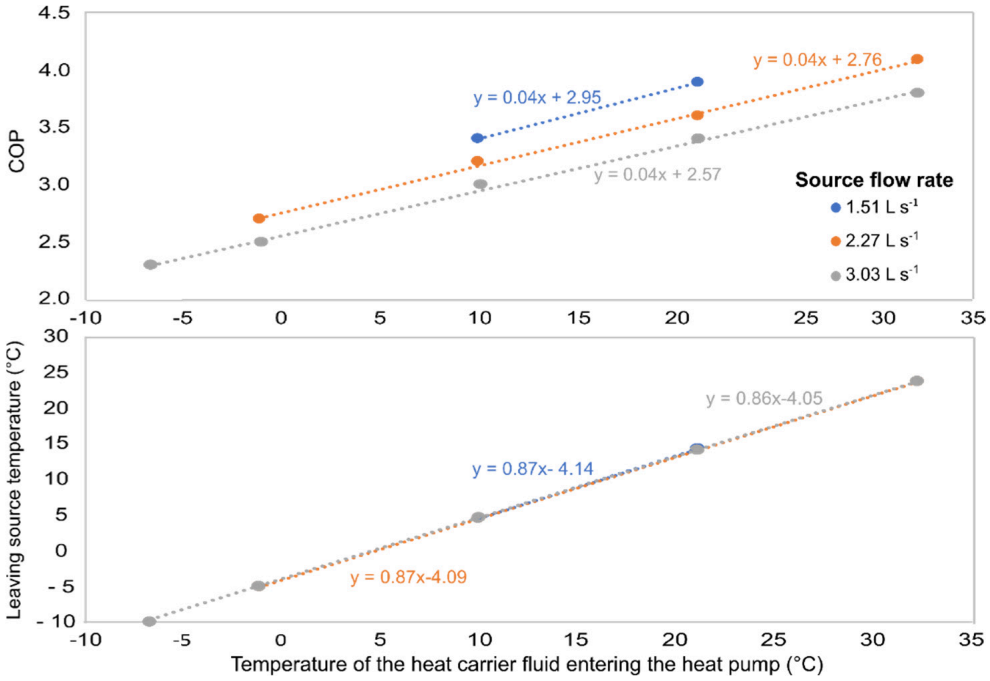

Figure 4. Linear regressions used to calculate the *COP* and *LST* in heating mode (HT180-Geosmart heat pump). Data points and regression lines overlap on the bottom graph. The manufacturer warns against using values outside the range of heat source temperatures presented here. The source flow rate corresponds to the flow rate of the fluid entering the heat pump on the source side (exiting from the previous heat pump or from the DBHE or plate heat exchanger in the case of the doublet).

Table 3. Assumptions made for the heat pump system. Based on low-temperature heating systems (leaving load temperature of 43 to 50 °C).

Parameter	Value
Heating mode	
Entering load temperature (ELT on Figure 1)	37.8 °C (100 °F)
Load fluid flow rate (LLT on Figure 1)	2.27 L s^{-1} (36 gpm)
Cooling mode	
Temperature of the return load fluid	21.1 °C (70 °F)
Load fluid flow rate	1.51 L s^{-1} (24 gpm)

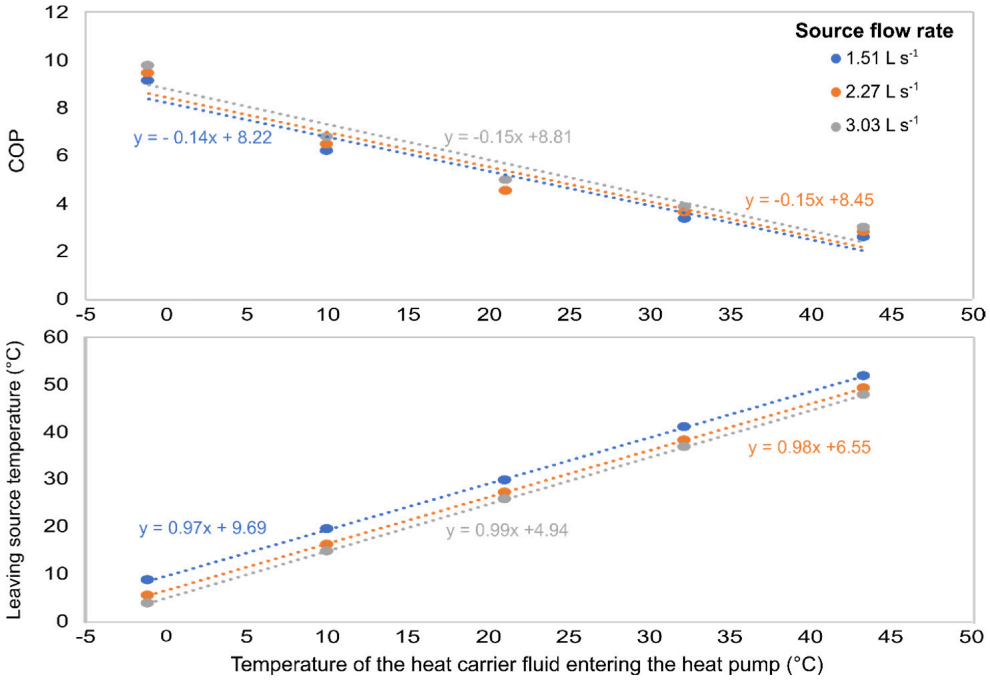

Figure 5. Linear regressions used to calculate the *COP* and *LST* in cooling mode (HT180-Geosmart heat pump). The manufacturer warns against using values outside the range of heat source temperatures presented here. The source flow rate corresponds to the flow rate of the fluid entering the heat pump on the source side (exiting from the previous heat pump or from the DBHE or plate heat exchanger in the case of the doublet).

4.3. DBHE

4.3.1. Characteristics of the System

For the illustrative example, an unused gas exploration well (called "A250") located in the municipality of Bécancour in the province of Québec (eastern Canada) was selected. It is set to be repurposed as a 1040 m coaxial DBHE (Appendix B.1). This involves introducing an inner and outer pipe into the existing well to form the DBHE, and filling the annular space between the existing casing (or rock in the deepest part of the well) and the DBHE outer pipe with grout (Figure 6). As this well was used for brine extraction for many years, it still contains a production pipe that would need to be removed first. The design and dimensions used for this DBHE are based on the optimum configuration for a repurposed O&G well with a short casing, as demonstrated in Gascuel et al. [6], and are presented in Figure 6 and Table 4. The heat carrier fluid is considered to be a mix of 70% water and 30% propylene–glycol to allow the DBHE to operate at very low temperatures (down to −10.1 °C) in order to maximize heat extraction with several heat pumps.

Table 4. Characteristics of the grout and pipes used for the DBHE model.

Categories	Material	Thermal Conductivity	Outer Diameter	Inner Diameter	Thickness
		(W m^{-1}K^{-1})	**(mm)**	**(mm)**	**(mm)**
Grout	Cement	0.7	156	114.3	21
Pipes					
Outer	Steel	54	114.3	102	6.1
Inner	High density polyethylene (HDPE)	0.4	60.3	48.6	5.87

The properties of each rock unit were considered homogeneous and isotropic in this example, and are presented in Appendix B.2.

This DBHE is combined with two heat pumps, connected in series (see Figure 1). The existence of auxiliary heating and cooling is assumed, allowing the assessment of scenarios in which the DBHE system does not meet the entire heating or cooling demand.

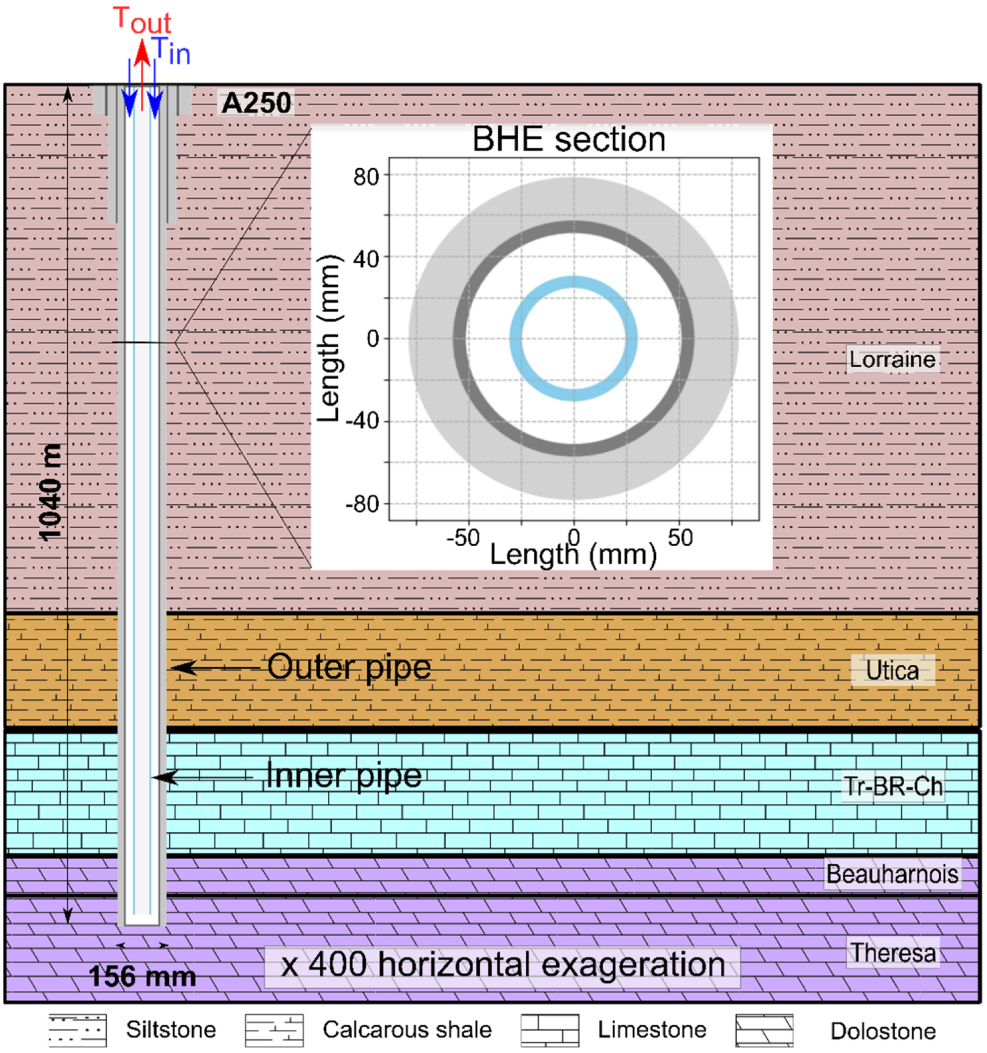

Figure 6. DBHE considered in the illustrative example involving the repurposing of an idle well. The lithologies correspond to simplified units for the Bécancour area (QC, Canada).

4.3.2. Numerical Model

The 3D FEFLOW model has a size of 400 × 400 m horizontally and extends vertically to a depth of 1600 m (well below the bottom of the DBHE). It is divided into eight distinct horizontal geological units based on the local geology, and some units shown in Figure 6 were subdivided. Boundaries were tested to ensure that they would not affect the results. The chosen mesh is presented in Appendix B.3. The portion of the DBHE with a pre-existing casing and grout has been neglected for the modeling (e.g., [16,51,65]).

As no significant regional groundwater flow is expected to occur at depth in this region, this model uses the same value of hydraulic head (100 m, corresponding to pressurized conditions such as reported in Tran Ngoc et al. [66] on opposite lateral boundaries). To speed up the simulations, the groundwater viscosity was considered constant, while its density was considered to vary linearly with the temperature. A constant temperature of 8 °C was imposed at the model surface boundary (representing an annual average) and a

constant heat flux of 53 mW m^{-2} as assigned at the base of the model, allowing equilibrium temperature measurements to be reproduced at the corresponding depths. The hydraulic and thermal properties assigned to the geological units are provided in Appendix B.2.

4.3.3. Preliminary Evaluation of System Heating and Cooling Capacities

Heating Season

DBHE operation using well A250 characteristics was first simulated for 212 days for pre-dimensioning, with a constant inlet temperature of −10.1 °C for different flow rates ranging from 1 to 6 L s^{-1} (see Section 2.5.1). A fluid flow rate of 5.24 L s^{-1} was found to maximize the net energy produced during a heating season (Figure 7A), and was thus considered to be the maximum usable flow rate for this DBHE. The heat pumps selected for the simulations were, however, limited to a maximum flow rate of 3.03 L s^{-1} (48 gpm) on the source side. Thus, if the heat pumps are connected in series on their source side, as presented on Figure 1, the maximum usable flow rate is only 3.03 L s^{-1}. This value was used as the maximum fluid flow rate for heating in the dynamic simulations presented in this paper.

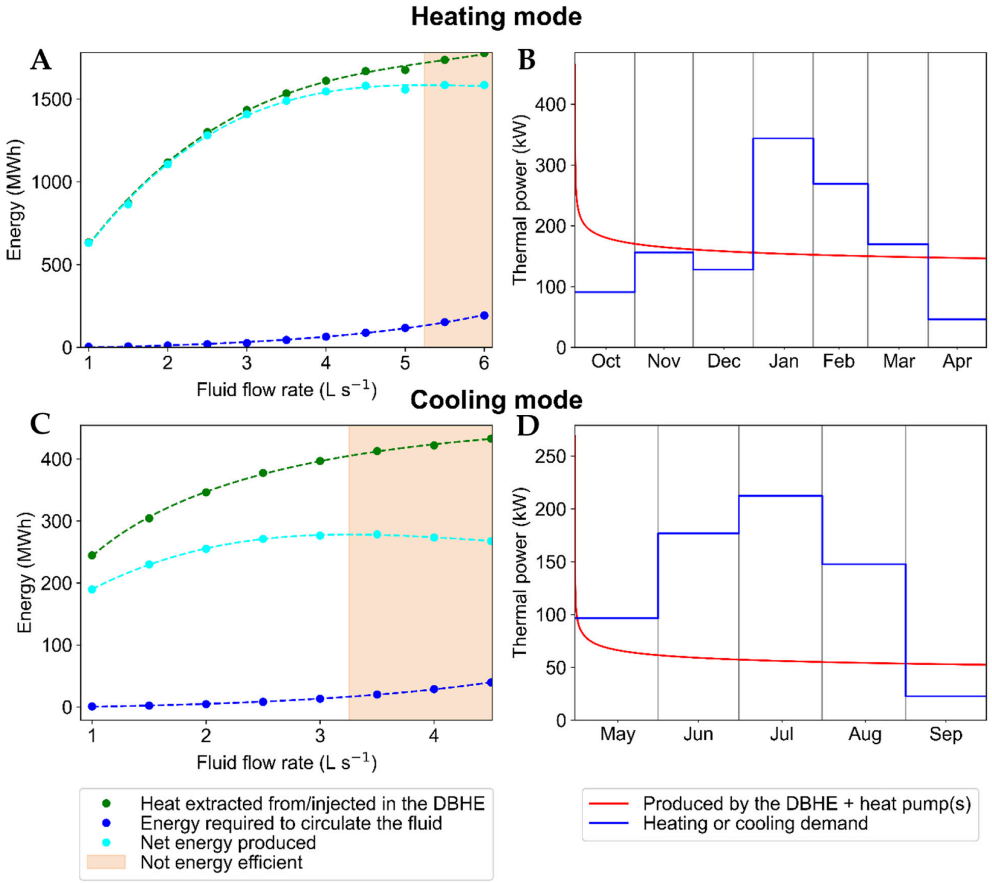

Figure 7. Results from the preliminary evaluation of the DBHE. (**A**) Heat and net energy produced and consumed by the DBHE in heating mode for various flow rates. Calculations based on a 212-day simulation (duration of the heating season) with a constant injection temperature of −10.1 °C and a constant fluid flow rate. The net energy produced is the difference between the amount of heat extracted and the energy required to circulate the fluid. (**B**) Heat produced at the maximum flow rate (3.03 L s^{-1}) compared to the greenhouse heating demand. (**C**) Cold and net energy produced and consumed by the DBHE in cooling mode for various flow rates. Calculations based on a 153-day simulation (duration of the cooling season) with a constant injection temperature of 47.7 °C and a constant fluid flow rate. (**D**) Cold produced at the maximum flow rate (3.03 L s^{-1}) compared to the greenhouse heating demand.

Tests were carried out to verify that the outlet temperature of the DBHE remains above the −6.7 °C security threshold when using this flow rate, even if the very low injection temperature of −10.1 °C is maintained throughout the entire heating season. An outlet temperature of −2.5 °C was recorded after 212 days of operation with a flow rate of 3 L s^{-1}.

With the constant inlet temperature and flow rate used here, the simulated heat production of the system (DBHE + heat pumps) declined rapidly in the first few days of operation, and then at a slower pace (Figure 7B). Although this preliminary simulation only provided a rough estimate of capacities, it clearly shows that this system would not be able to satisfy the entire heat demand of the 4000 m^2 reference greenhouse (Figure 7B).

Cooling Season

The same process was repeated for the cooling season. However, the fluid was here injected in the inner pipe and returned to the surface using the annular space between the pipes. A constant inlet temperature of 47.7 °C was used and the optimum fluid flow rate calculated was 3.3 L s^{-1} (Figure 7C), a lower value than that obtained for the heating season, but again, higher than the flow rate the heat pumps can handle. Thus, the fluid flow rate of 3.03 L s^{-1} (48 gpm) was also used as the maximum fluid flow rate for cooling in all simulations for the DBHE.

Unsurprisingly, the cooling capacity of the DBHE is lower than its heating capacity; a maximum of 397 MWh can be injected into the subsurface during the cooling season (5 months; Figure 7D), whereas 1436 MWh can be extracted during the heating season (7 months; Figure 7B) when the DBHE is operated at 3.03 L s^{-1} in both modes, which corresponds to 3 times less.

4.3.4. Scenarios for Conventional Simulations

The heating and cooling demand of the building (greenhouse) is greater than the heating or cooling capacity of the DBHE. The two scenarios for boundary conditions were used for the DBHE to investigate the limits of the conventional simulation approach (Section 3). Figure 8 illustrates the monthly patterns of heat extraction and injection used in time series 1 and 2. In time series 2, the heat extraction in December to March and heat injection from May to August included were limited based on the results of the preliminary simulation. The same *COP* values were used to define the heat extraction time series in both scenarios (Time series 1 and 2).

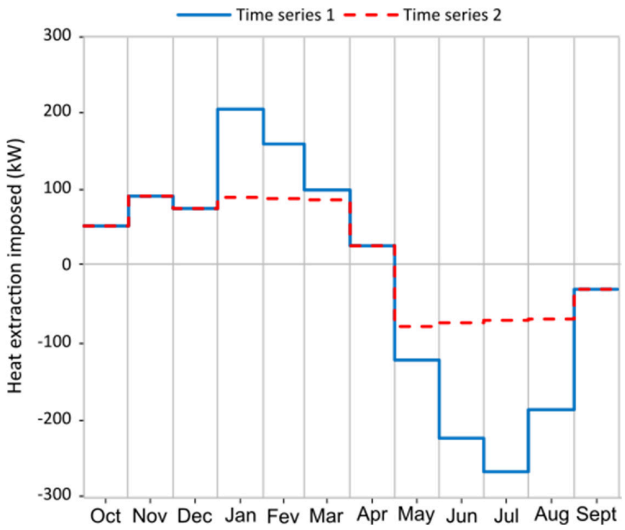

Figure 8. Heat extraction imposed on the DBHE in the conventional simulations for the two scenarios described in Section 3. The positive values correspond to heat extraction, while the negative values correspond to heat injection.

4.3.5. Results of the Dynamic Versus Conventional Simulations

First, dynamic simulations were run using the codes developed to control the DBHE operation to model the heating and cooling operation of the greenhouse. Code 1 and Code 2 have one and two heat pumps available for cooling, respectively. The results for the first year of these 30-year simulations were compared to those obtained using a conventional approach (i.e., non-dynamic) using pre-defined time series of heat extracted or injected for the DBHE, for the two scenarios presented in Section 3. In agreement with Figures 7 and 9, this confirms that the DBHE is unable to fulfill the entire heating or cooling demand in peak demand periods. The codes take this into account by simulating the heat pumps with a maximum number of activated heat pumps (two) and maximum fluid flow rate during these periods. Thus, heat extraction or injection is limited by the capacity of the heat pump system under consideration (this occurs in both winter and summer, as the DBHE system is undersized for the greenhouse) and by the safety thresholds imposed on the *EST* of the second heat pump.

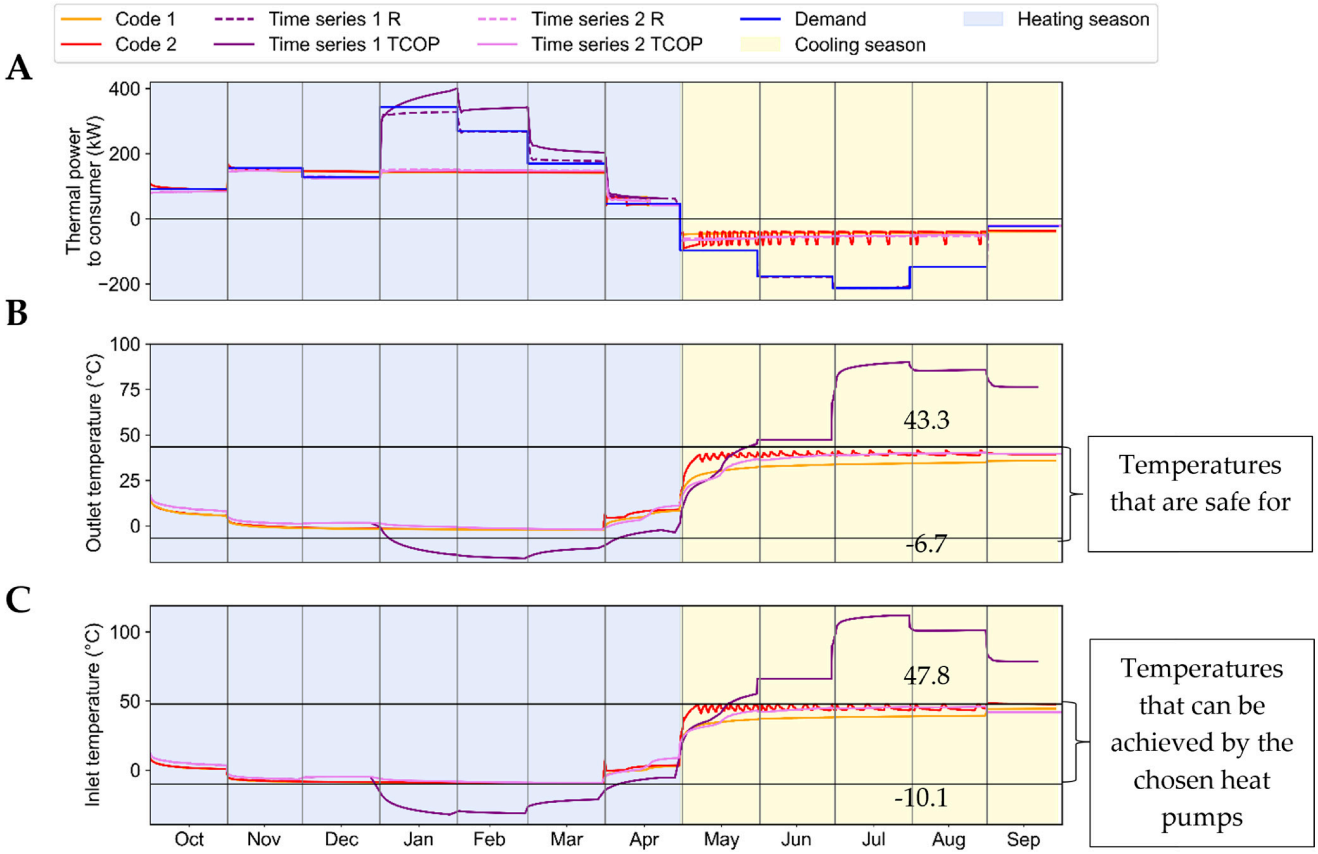

Figure 9. (**A**) Heating and cooling power production calculated for the dynamic approach with the codes and for the conventional approach using the different pre-defined time series for the first year of operation. Positive values correspond to the heating power and negative values to the cooling power. (**B**) Simulated outlet temperature of the DBHE for the first year of operation. (**C**) Simulated inlet temperature of the DBHE for the first year of operation. Notes: Values on this graph correspond to the combined use of the DBHE and heat pumps. The period starts at the beginning of the first heating season, in October. The results for Code 1 and Code 2 are superposed from October to the end of April. The results from time series 1 and 2 are superposed from October to the end of December.

In Codes 1 and 2, the system operates in October at the maximum allowed flow rate of 3.03 L s^{-1} with only one heat pump activated. The results show that with this setup, the system would be able to fulfill the heating demand in October, with some surplus production at the beginning of the month. Indeed, in the first few hours of the

simulation, the heat production corresponds to 157% of demand, but quickly falls to 112% in the first few days, and then decreases gradually toward a slight underproduction (i.e., 98% of demand at the very end of the month). The second heat pump is activated on 1 November due to the increase in heating demand, and this allows for a sharp increase in heat production (Figure 9A). The heat production decreases as the rocks around the DBHE are cooled, and, around 3 November, the system is no longer able to meet the full heat demand. As all the available heat pumps are activated and the flow rate is at the maximum defined for this system, the heat production cannot be increased further.

In December, the heat demand for the greenhouse is lower, but still requires both heat pumps that are maintained at a flow rate of 3.03 L s^{-1}. The heat demand then increases from January through March, but the system is already operating at its maximum capacity. The heat production from the DBHE system decreases slightly over the winter as the rocks surrounding the DBHE are cooled. In Codes 1 and 2, the minimum *EST* temperature reached during the simulations at the end of March for the second heat pump is −5.96 °C, above the security threshold of −6.70 °C (Figure 9C). It is therefore not necessary to deactivate the second heat pump.

The heat demand decreases in April. To avoid wasting energy, the code lowers both the number of activated heat pumps (to one) and the flow rate. This leads to an increase in inlet temperature, thus leading to an increase in the outlet temperature of the DBHE. As the temperature of the fluid exiting the DBHE gets higher (Figure 9B), the efficiency of the heat pump increases, resulting in greater heat production. Thus, the flow rate is decreased a second time later in April to limit energy consumption and the overproduction of heat.

The cooling capacity of the DBHE system is already lower than the cooling demand in May. In both Code 1 (one heat pump activated) and Code 2 (two heat pumps activated), the system is therefore already operating at maximum capacity at the start of the cooling season, meaning that the maximum flow rate is used. The system is far from being able to meet the cooling demand during the warm season, even in early May. As heat is injected underground, the temperature of the DBHE and surrounding rocks increases rapidly, leading to a sharp increase in both the outlet and inlet temperatures of the DBHE. In Code 2, after a few days, the *EST* of the second heat pump (corresponding to the *LST* of the first heat pump; see Figure 1) exceeds the safety threshold of 43.3 °C. The second heat pump is thus deactivated, leading to a decrease in both inlet and outlet temperatures as less heat is injected underground. This decrease in temperature prompts the second heat pump to be reactivated, but it is quickly deactivated as the safety threshold is reached once again. This pattern repeats itself until the end of August (corresponding to the sawtooth portion of the curve in Figure 9). The periods during which the second heat pump is activated become both shorter and further apart as the rocks surrounding the DBHE get warmer. In September, the cooling demand decreases. The system is then able to meet demand in both Code scenarios. Code 2 specifies the use of only one heat pump, with the lowest allowed operation flow rate of 1.5 L s^{-1}.

Time series 1 and 2 consider a constant *COP* (with different *COP* for heating and cooling) and do not consider the limitations of the heat pumps (heat pump's heating capacity or *EST* security thresholds). In October, November and December, the heating demand is moderate. In both Time series 1 and 2, the heat production, if calculated using the fixed *COP* used to define the imposed heat extraction (R), corresponds to the heat demand. However, if the *COP* is recalculated according to the simulated outlet temperature (in TCOP), which is more realistic as the *COP* is known to vary with the heat source temperature, this *COP* would be higher than the fixed *COP* from October to December, leading to lower overall heat production (see Section 2.3). Then, in time series 1, the heat

extraction imposed in January is higher than the DBHE capacity. As the model attempts to fulfill the heating demand, the simulated inlet and outlet temperatures of the DBHE decrease drastically, The *LST*s is well below what can be achieved by the heat pumps, while the *EST*s decreases below the minimum temperature at which heat pumps can operate safely (Figure 9B,C). Furthermore, the way the power boundary condition is coded in FEFLOW (inlet temperature adjusted at each time step considering the outlet temperature and power boundary condition) causes numerical instability and potential numerical errors. Then, in May, as the cooling season begins and heat is injected in the DBHE, the inlet and outlet temperatures of the DBHE increase. Because of the very low inlet and outlet temperatures simulated previously, in early May, the inlet and outlet temperatures simulated in time series 1 are lower than those simulated in Codes 1 and 2. However, the inlet and outlet temperatures continue to rise. From early June to late September, the inlet and outlet temperatures simulated are well above the temperatures at which the heat pump could operate safely (Figure 9B,C).

In Time series 2, the inlet and outlet temperatures remain within a reasonable range in the context of heat pump operation (Figure 9B,C). The difference between the fixed (Results R) or recalculated *COP* (Results TCOP) is smaller than in time series 1. However, the heat production with a recalculated *COP* remains below demand during the months when the system should have been able to fulfill the entire heat demand (e.g., October). The effect would be greater if there were no prior knowledge of the expected *COP* (the thermal power extraction values in Time series 1 and Time series 2 were defined using the average heating and cooling *COP*s simulated in Code 1).

Nonetheless, as the heat pumps are not considered individually in Time series 1 and 2 (unlike with dynamic simulations), it is impossible to know when the second heat pump is activated. When the second heat pump is activated, then its *EST* becomes the *LST* of the first heat pump (see Figure 1), meaning that it is lower than the outlet temperature of the DBHE during the heating season, and higher during the cooling season. This would result in the *COP* for the second heat pump being lower than that calculated using only the linear regression and the simulated outlet temperature. Thus, the recalculated *COP* (results TCOP) for Time series 1 and 2 is overestimated during these periods, although it is unknown by how much.

4.4. Geothermal Doublet

4.4.1. Characteristics of the System

Two existing wells, A250 and A239, are assumed to be repurposed as production and injection wells, respectively (similar to Gascuel et al. [67]). The well A250 is a 1040 m deep vertical well, with an open section between 785.5 and 1040 m depth, having a diameter of 156 mm. Well A239 is also vertical and slightly shorter (931.6 m depth), with an open section between 767.6 and 931.6 m depth and a diameter of 140 mm (Figure 10). The open sections of both wells intercept the Tr-BR-Ch geological unit (regrouping the Trenton, Black-River and Chazy geological groups), which has been shown to be permeable in previous studies [66]. The well A250 also reaches the top of the underlying Beauharnois unit. Detailed characteristics of the two O&G wells to be repurposed are given in Appendix B.1. The properties of the rock units, considered homogeneous and isotropic in this example, are presented in Appendix B.2.

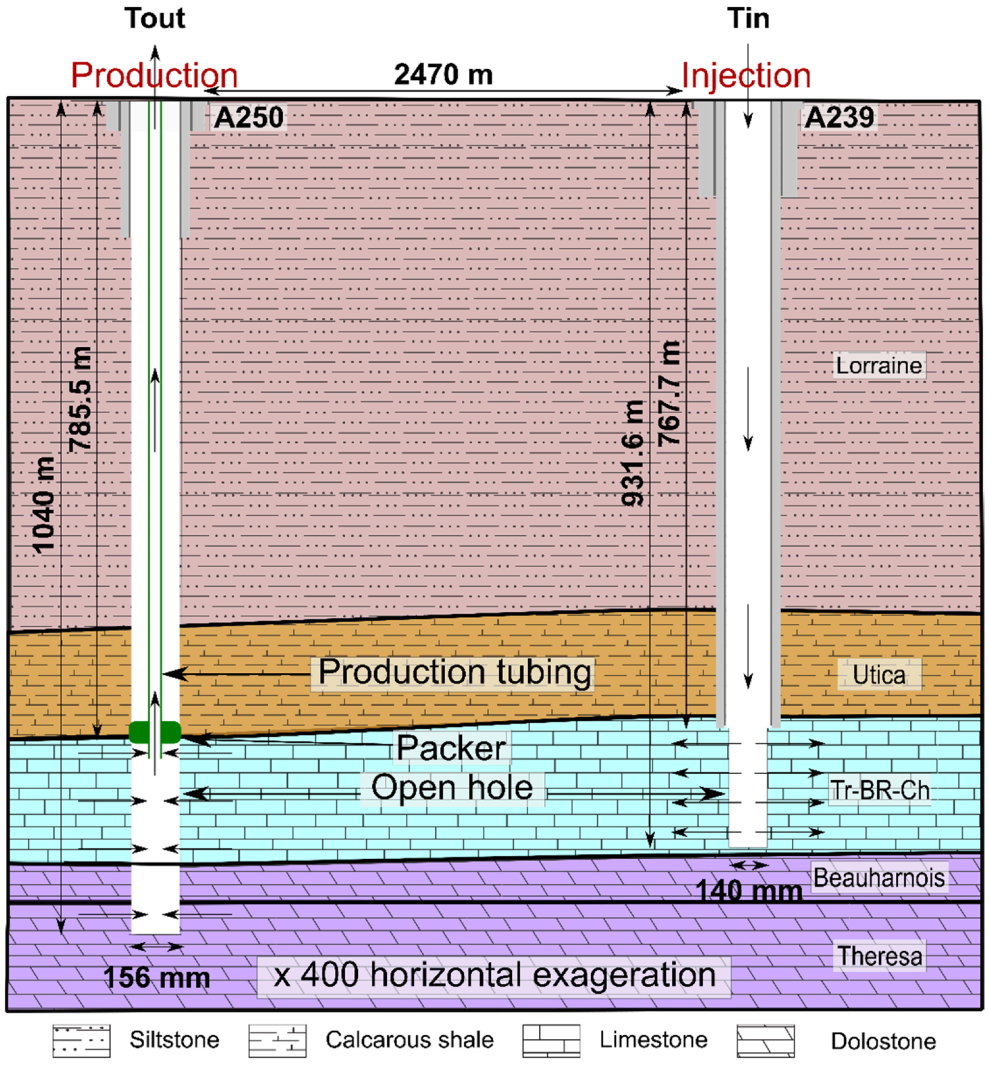

Figure 10. Doublet considered in the illustrative example using two idle existing wells. The lithologies correspond to simplified units of the Bécancour area.

4.4.2. Numerical Model

The model is built with the same eight distinct units as the DBHE model. The geological model of Claprood et al. [68] was used to define the geometry of the FEFLOW model (see Appendix B.3). In this example, the Yamaska and Deschambault faults were considered impermeable, although evidence for and against the Yamaska Fault being a hydraulic barrier has been presented [69,70]. Both the brine density and viscosity were assumed to vary in the model. Relationships predefined in FEFLOW for variable viscosity and the non-linear dependency of density on temperature in FEFLOW were used (same as in Gascuel et al. [13] see Appendix B.2). The reference temperature, density and viscosity of the brine were set at 31 °C, 1068 kg m^{-3} and 1.742 × 10^{-3} Pa s, respectively.

4.4.3. Preliminary Evaluation of System Heating Capacity

Preliminary simulations of the doublet were run with injection temperatures of −4 °C (just above the brine's freezing point) and 10 °C, testing various flow rates for each injection temperature. The maximum hydraulic heads obtained in the preliminary simulations, corresponding to the end of the last heating season, were plotted against the associated flow rates during the heating seasons (Figure 11A). Based on a linear regression, the maximum allowable flow rate to prevent the injection hydraulic head from exceeding 500 m would

be 2.84 L s^{-1} if the injection temperature is kept at 10 °C, but it would be 2.15 L s^{-1} if the brine is reinjected at −4 °C.

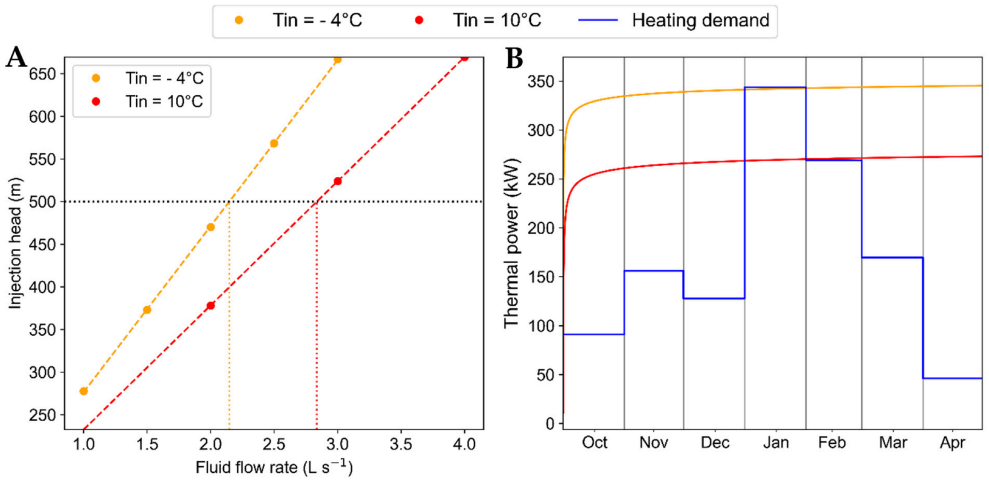

Figure 11. Results from the preliminary evaluation of the doublet. (**A**) Simulated hydraulic heads in the injection well at the end of the 30-year period for various flow rates and two injection temperatures (10 °C and −4 °C), used during the heating season (212 days/year in this example) but shut down for the rest of the year (no cooling is considered for the doublet). (**B**) Thermal power production at the maximal allowable flow rate (respectively, 2.84 L s^{-1} and 2.15 L s^{-1} for injection temperatures of 10 °C and −4 °C) along with the heating demand, compared for the first heating season only. In these very simple simulations with constant flow rate and injection temperature, heat production remains almost identical each year.

Simulations with the injection temperature of −4 °C and 10 °C and the corresponding maximum allowable flow rate were run (Figure 11B). The geothermal doublet produces about 30% more thermal power with an inlet temperature of −4 °C than with the inlet temperature of 10 °C, despite the lower flow rate. However, the injection temperature of −4 °C would imply the use of more heat pumps in series or heat pumps of a larger capacity, which would consume more energy (an increase greater than the pumping energy saved by using a lower flow rate). As can be seen from Figure 11B, this geothermal doublet operating with an inlet temperature of 10 °C would be enough to fulfill the greenhouse's heat demand for the entire heating season, except for the month of January (the coldest), when a lower injection temperature would have to be used. The maximum flow rate obtained with the injection temperature of 10 °C (2.84 L s^{-1}) was thus selected and imposed as the maximum flow rate allowed in the brine loop in the dynamic simulation for this example.

4.4.4. Results of the Dynamic Simulations Versus Conventional Approach

Similarly to the DBHE, the heating operation of the greenhouse was also simulated using both approaches (dynamic and conventional) for comparison: (1) the Python code (scenario called "Code", i.e., under dynamic conditions) that considers heat pumps individually and (2) the predefined time series (Time series as defined in Section 3) to control its flow rate during operation. The results from both approaches show that the doublet could fulfill 99% of the heating demand (Figure 12A), while not reaching the injection head limit of 500 m after 30 years (Figure 13C). However, the simulations and results differ in many aspects.

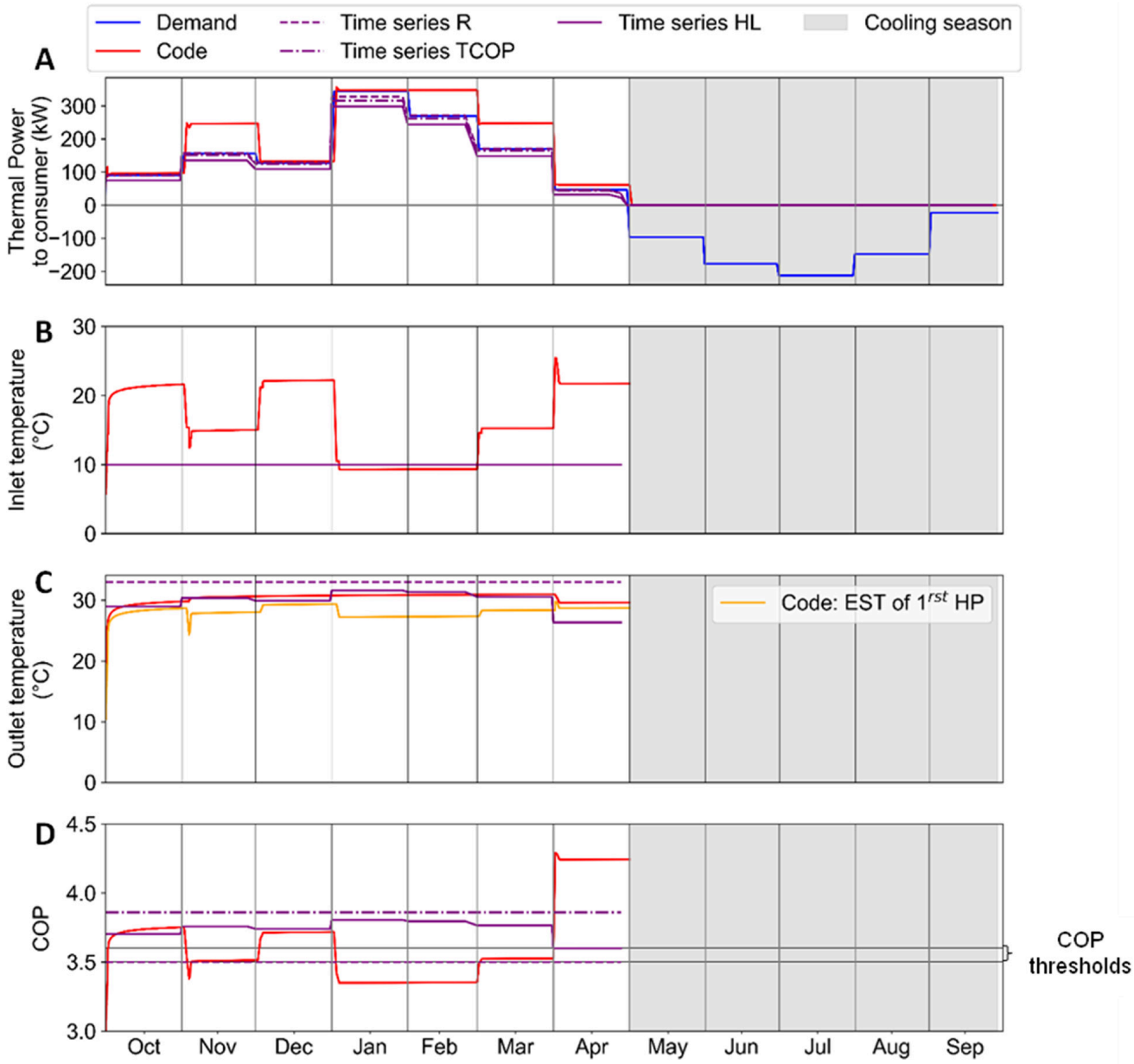

Figure 12. Comparison of the results obtained for the 30th year of operation with the dynamic simulation and with the conventional approach (using different ways of post-processing the simulation results, see Section 3): (**A**) Thermal power production and demand. The thermal power to the consumer is null in summer in both the code and time series simulations during the cooling season, thus the curves are superposed. (**B**) Inlet temperature in the doublet, (**C**) outlet temperature of the doublet and *EST* of the first heat pump, and (**D**) average *COP* of the active heat pumps (for the dynamic simulation) or heat pump *COP* used to calculate the thermal power (for the conventional approach).

In the Code scenario, the flow rate in the intermediate loop is at 2.27 L s^{-1} in October, with only one activated heat pump necessary to fulfill the heating demand (Figure 13A,B). The flow rate in the brine loop is increased during the first hours to increase the *COP* of the heat pump by providing more heat to the plate heat exchanger (Figures 12D and 13A). The production well gradually heats up as warm brine is pumped into it, and the temperature of the brine reaching the surface increases (Figure 12C). In November, the heat demand increases (Figure 12A). The flow rate in the intermediate loop increases to its maximum value of 3.03 L s^{-1}, and a second heat pump is activated (Figure 13B). The average *COP* of

heat pumps falls under the threshold of 3.5 with the activation of the second heat pump (Figure 12D). As a result, the code increases the brine flow rate up to the maximum flow rate defined for the brine loop in preliminary simulations (2.84 L s^{-1}; Figure 13A). In December, the heat demand decreases (Figure 12A). The second heat pump is deactivated, leading to an average *COP* over the threshold of 3.6 (Figures 12D and 13B, see Section 2.6.4). However, heat production at the same brine flow rate is just slightly higher than heat demand (under the 10% threshold; Figure 12A). Thus, the code maintains the same brine flow rate (Figure 13A). In January, heat demand peaks (Figure 12A). Three heat pumps are activated and both the flow rates in the brine loop and intermediate loop are kept at their maximum (Figure 13). The average *COP* of the heat pumps is lower than in previous months (around 3.3; Figure 12D), but the system is still able to meet demand (with a slight overproduction; Figure 12A). In February, the demand is still high; deactivating a heat pump or reducing the flow rate to the next fixed flow rate of 2.27 L s^{-1} in the intermediate loop would result in a heat production lower than the demand by more than 10%, and is thus not allowed by the code. The system thus continues to operate with three heat pumps and maximum flow rate. In March, the heat demand decreases (Figure 12A). The third heat pump is deactivated, but the flow rates in the intermediate and brine loop are kept at their maximum (Figure 13). The system overproduces heat in March due to the integer number of heat pumps and fixed flow rate values in the intermediate loop (Figure 12A). The condition of an average *COP* higher than 3.6 (see Section 2.6.4), which would prompt the brine flow rate to be reduced, is not achieved (Figure 12D). Finally, as heat demand is low in April, a single heat pump is activated to limit overproduction and electricity consumption, and the minimum defined flow rates are used in both the brine and intermediate loops (Figure 13). From May to October, there is no heat demand, and the system is shut down. In the Code scenario (Figure 12), the doublet system overproduces heat during most of the heating season. This is due to the choice of threshold used to activate or deactivate a pump and change the intermediate loop flow rate. The system is not allowed to under-produce by more than 10% if there is capacity to produce more heat safely, but activating another heat pump or increasing the flow rate to the next allowed value generally leads to a greater increase in the production than those at 10%. Reducing the heat production by decreasing the flow rate in the brine loop is only allowed by the code if the average *COP* of the activated heat pumps is greater than 3.6, a condition that was only achieved when a single heat pump was activated (months of October, December, and April; Figures 12D and 13B).

All simulations using the conventional approach (Time series R, TCOP and HL) provide similar results. As far as Time series R results are concerned, the thermal power supplied to the consumer in the time series controlled simulation seems to correspond exactly to its heat demand (Figure 12A), with the exception of in January, when a flow rate of 2.84 L s^{-1} (maximum safe flow rate according to the preliminary simulation) had to be imposed to avoid reaching an excessively high injection head during operation, as the capacity of the systems is large enough to fulfill the demand (see Section 4.4.3). However, not accounting for heat losses or the temperature-dependent *COP* (Time series R) is not realistic. Considering the recalculated *COP* instead of a fixed *COP* to interpret the results, but not the heat losses in the production well (Time series TCOP), revealed slight differences between the produced thermal power and demand. When both the heat losses and a recalculated *COP* are considered (Time series HL), it can be seen that the heat production simulated using the conventional method is always lower than the demand, even though the system would be able to fulfill the demand according to both the preliminary evaluation and the Code scenario (Figure 12A). The recalculated temperature at the outlet of the production well in Time series HL is of a similar range to that in the Code scenario, in

which the temperature loss is calculated during the simulation itself (Figure 12C). Despite this, the calculated temperature losses are not the same, as temperature loss is controlled by the flow rate over time, and the flow rates in these simulations differ. This shows the clear advantage of using a code to run dynamic simulations that consider heat pumps individually and can make adjustments during a simulation, rather than using pre-defined time series.

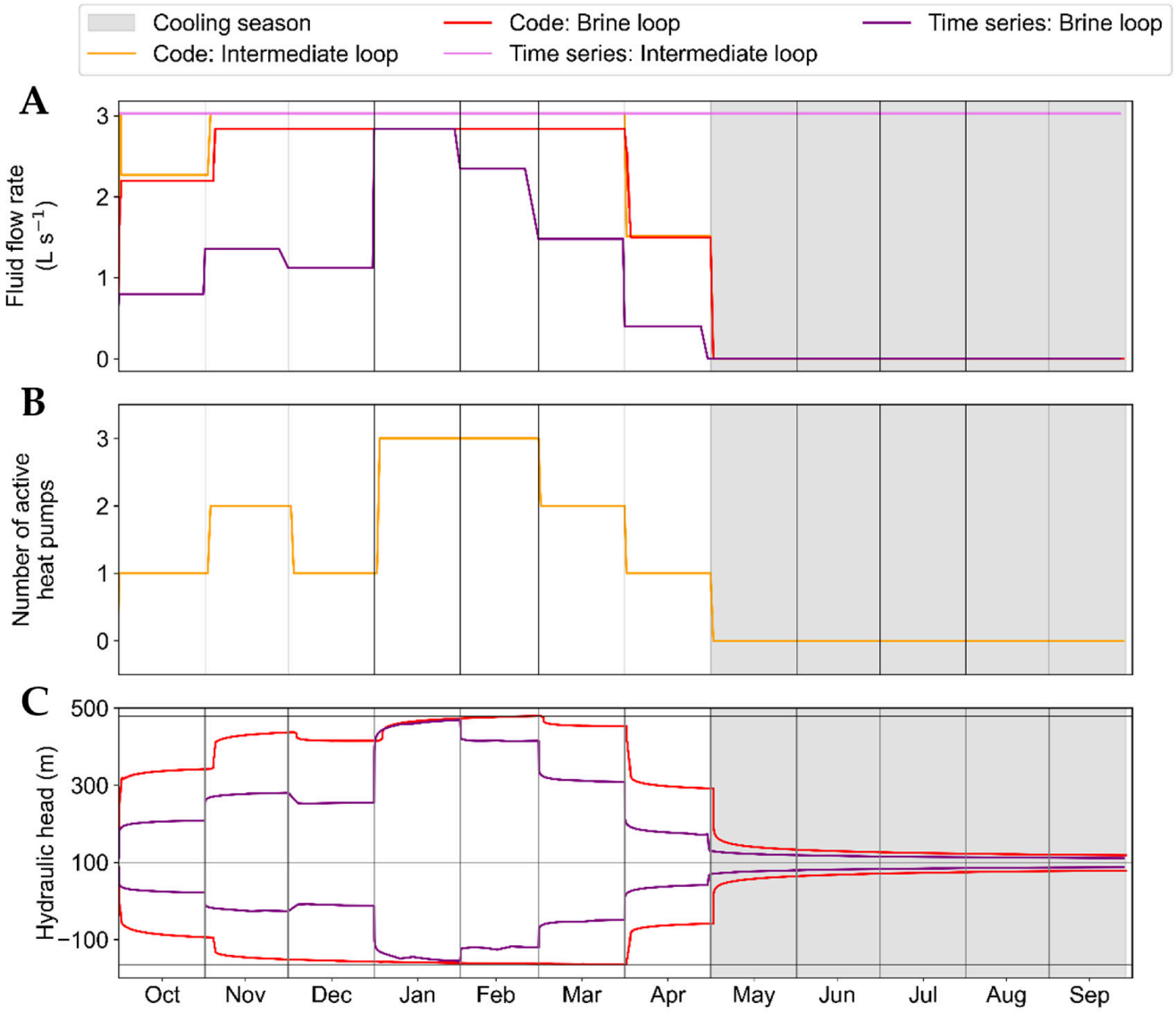

Figure 13. (**A**) Fluid flow rate, (**B**) number of active heat pumps and (**C**) hydraulic heads in the wells (with values > 100 m corresponding to the injection well, and values < 100 m to the production well) during the 30th year for the dynamic simulations and the various scenarios of a conventional approach using a pre-defined time series for the doublet. The fluid flow rate in the intermediate loop in the dynamic simulation is superposed to the pink line representing the flow rate in the heat pump in the predefined Time series simulation from November to March, then to the flow rate in the geothermal doublet in code-controlled simulations in April.

5. Discussion

The approach presented here couples 3D numerical models capable of representing the operation of either geothermal doublets or DBHEs with the use of one or several heat pumps, while considering a variable heating/cooling demand profile for a specific building over the course of a year. It considers several important aspects, such as the optimum

number of operating heat pumps and their temperature-dependent *COP*. The various codes developed also contain functions to consider and/or calculate: (1) temperature-dependent fluid properties, (2) the possibility to adjust heat production by changing the flow rate and/or activating or deactivating heat pumps, (3) the temperature range in which the heat pumps can operate safely and their limited capacity, (4) a maximum sustainable flow rate, (5) heat losses by conduction in the production well of the doublet, and (6) the imperfect heat transfer through the plate heat exchanger of the doublet system. This approach thus allows dynamic simulations to be carried out, enabling each component of the system (surface and subsurface) to adapt to the results of the other during the simulation. As the 3D models of geothermal systems have been developed in FEFLOW, this offers a wide range of possibilities to consider geological stratification and features, system configurations, and boundary conditions.

The results obtained with this method for the Bécancour area, including inlet and outlet temperatures, *COP* and thermal power, were compared against the results of a conventional approach using pre-existing tools in FEFLOW (i.e., pre-defined time series, without using the Python codes developed). While the various values assigned to properties and condition thresholds (e.g., to activate and deactivate heat pumps and adjust flow rates) are specific to the Bécancour case study, the results clearly highlight the advantages of the dynamic simulation approach. With the conventional approach, the boundary conditions controlling the heat extraction or injection in the DBHE or doublet must be set before the simulation begins. Consequently, with this approach the temperature dependence of the *COP* cannot be considered when estimating the amount of heat to be extracted or injected. While a temperature-dependent *COP* can be recalculated after the simulation, it introduces differences between simulated heat or cold production and demand, even at times when the system should be able to cover the demand. Furthermore, as the conventional approach does not consider heat pumps individually, when several heat pumps are activated, the recalculated *COP* is overestimated as it is calculated from the outlet temperature of the geothermal system, which does not correspond to the *EST* of the second or third activated heat pump. Additionally, the conventional approach fails to account for the imperfect heat transfer through the heat exchanger in the doublet system, which contributes to the overestimation of the recalculated *COP*. The codes developed to perform dynamic simulations take these issues into account, integrating the calculation of time-dependent *COP* and heat losses by conduction in the production well for the doublet system, and heat transfer through the plate heat exchanger during the simulation itself, allowing the required heat extraction or injection to be estimated more realistically.

Another limitation of the conventional approach is that the temperature thresholds below and above which the heat pumps must not be operated cannot be considered. This consideration is particularly important when the geothermal system is unable to meet the building's full demand. This is the case for the DBHE in our example, which is expected to be representative of many hybrid systems currently in operation, in which the geothermal component is intentionally undersized to reduce installation costs. This problem can be partially solved by using prior knowledge of the system's capacity to limit the heat extraction or injection imposed. However, dynamic simulations provide a more representative value of the thermal power that can be injected or extracted at a given time in the simulation as a function of demand. This is calculated at each time step so that the operation conditions can be adjusted accordingly.

It must be noted that the simulations with the conventional approach were not significantly faster than the code-controlled simulations, as FEFLOW changes the inlet tem-

perature in the DBHE or the flow rate in the doublet at each time step to fulfill the time series-controlled boundary conditions.

As mentioned in the Introduction, the dynamic coupling between heat pump and geothermal system models has already been implemented in a few studies and for different conditions (e.g., [32–34,40]). However, these involved various assumptions (simplifications) or different conditions, including a single-stage heat pump allowing for only one value of flow rate in the system; the system's ability to fulfill the entire heating or cooling demand; shallow systems that do not need to consider heat transfer by conduction; and/or the temperature independence of the brine properties in the doublet. The codes developed here offer greater flexibility in simulating system operation. They allow the simulation of cases where the following pertains:

- only part of the demand would be covered by the geothermal system, with auxiliary systems to help cover the peak loads (i.e., hybrid systems);
- several heat pumps can be connected in series and activated or deactivated according to demand, thereby optimizing system efficiency;
- the impact of temperature on the brine properties (density, viscosity and heat capacity) can be taken into account.

In particular, the temperature dependence of the viscosity of the injected brine in a doublet was found to have a significant impact on the simulated hydraulic head in the injection well, limiting the maximum sustainable flow rate and leading to higher power consumption to inject the brine under pressure when a low injection temperature was used [13]. The temperature dependence of the heat carrier fluid properties could not be accounted for in the numerical simulation of the DBHE (due to the limitations of the BHE tool in FEFLOW). Nonetheless, temperature dependence was considered in the surface system and when calculating pressure losses in the DBHE.

This dynamic approach represents a valuable new tool for better assessing the suitability of installing a geothermal system coupled with heat pumps, as it allows (1) the design of geothermal heat pump systems in a complex geological context, (2) the consideration of variable energy demand throughout the year, (3) the estimation of the heating/cooling production of the designed systems over time and thus the assessment of the need for auxiliary heating/cooling systems, as well as (4) the prediction of the required capacity and their energy consumption.

Although the codes have been developed so that they activate/deactivate heat pumps and/or modify the flow rate in a logical and consistent manner with regard to technical specifications, some of the thresholds used in the codes may need to be adjusted according to the needs and/or context of a given project. These include the following: (1) the 10% overproduction limit beyond which a change in the number of activated heat pumps or flow rate is considered, (2) the *COP* target of 3.5–3.6 for heat pumps in the doublet system and (3) the minimum brine flow rate in the doublet system. Some of these thresholds could be optimized and adjusted as studies are carried out to ensure the optimal operation of the systems. In addition, the control code could be further refined by improving the regressions performed on heat pump performance as a function of source-side temperature, to allow the use of intermediate flow rate values, which would allow greater flexibility in simulated heat pump operation (thus avoiding overproduction). Finally, as the analytical models recently developed to represent DBHEs are increasingly capable of simulating the subsurface system realistically (considering the layered geology, temperature gradient, etc.) (e.g., [71–73]), it could be interesting to couple the control code developed in this study with one of these refined analytical models instead of a numerical model as part of a future study.

6. Conclusions

In this study, Python codes designed to be used jointly with numerical models of geothermal systems have been developed to allow the dynamic simulation of DBHEs and geothermal doublets coupled with several heat pumps to meet the varying heating (and cooling for the DBHE) demand of a given building. Efforts have been made to approach realistic operation for these systems, integrating both subsurface features and the technical limits of the surface system components. This method allows the geothermal systems to be simulated under different conditions, including when they cannot meet the entire energy demand during peak load periods, a common design practice in the field where auxiliary systems are often installed to supplement geothermal systems during these periods. Furthermore, it allows several aspects to be considered simultaneously that are generally neglected in studies (even on an individual basis), including temperature loss in the production well, imperfect heat transfer in the plate heat exchanger, and the temperature dependence of fluid properties, all within the framework of dynamic simulations, enabling the different values to be recalculated at each time step.

The codes developed are intended to assist in the design of geothermal heat pump systems, especially for deep wells such as those presented in this study or BHEs requiring special attention in the modeling of their subsurface components. They allow the iterative adaptation of the system design or operating conditions to minimize input energy consumption while maximizing the heating/cooling (for the DBHE only) output performance. In addition, details on the number and operating schedules of heat pumps, electricity consumption, and required heating/cooling capacity of auxiliary systems and amount of energy they need to provide over a typical year could help establish reliable projections regarding the cost of these systems, and to optimize their cost-effectiveness.

The dynamic simulations conducted for the Bécancour case, involving the reconversion of O&G wells in the St. Lawrence Lowlands to provide energy to a bell pepper greenhouse, show that the heating power provided by the well doublet generally exceeds the consumer's needs, while it falls below for the months of February, March and April in the case of the DBHE. The comparison with the conventional approach showed that all three simplified well doublet scenarios (Time series R, TCOP and HL) provide similar results, with the simulated heat production consistently lower than the heating demand, while the system is shown capable of fulfilling the demand according to both the preliminary evaluation and the dynamic simulations considering more realistic operating conditions. In the case of DBHEs, one of the main issues is that the conventional approach overestimates the *COP* during the heating season, and it is not possible to determine the extent of this overestimation because the heat pumps could not be considered individually. In both cases, inaccurate estimates resulting from the inability to adjust parameters during simulations could lead to poor decision-making. Another major advantage of this approach is that heat production is subject to technical and safety constraints designed to better reflect the actual, variable conditions within the building, which results in more realistic operating conditions and energy production.

The developed codes have been made available to the scientific community and geothermal experts on GitHub. While the parameters set in the codes correspond to the case study used as an illustrative example (e.g., for the numerical models, heating and cooling demand profile, *EST* threshold for heat pumps and regression coefficients to calculate the *COP* and *LST* of heat pumps, characteristics of the production well and surrounding rocks to calculate temperature losses, efficiency of the plate heat exchange, and number of heat pumps), they can easily be modified to suit other case studies. The code could also be used in simulating systems whose demand varies over time (e.g., due to climate change) and which has an energy demand profile other than monthly,

with some additional modifications. The release of this code opens a wide range of possibilities for simulating the heat production of deep geothermal heat pump systems, with appropriate conceptualization of both the subsurface and surface components of the system.

Further work can be envisioned to integrate an economical module into the codes developed, activating and deactivating heat pumps and adjusting flow rates not only on energy produced, but also on the financial savings achieved. The postprocessing codes could also integrate an economic analysis module, allowing cost to be considered when selecting the best option.

Supplementary Materials: DBHE Dynamic simulation code—The python code referred to in the article, used to launch the simulations with the DBHE. This code was made available on GitHub; Doublet Dynamic simulation code—The python code referred to in the article, used to launch the simulations with the geothermal doublets. This code was made available on GitHub. Pertes de charge BHE—A code used to calculate head losses in the DBHE. This code was made available on GitHub. Properties mod—A code used to interpolate the properties of water and propylene–glycol and water solutions at various temperatures. It is required to run the DBHE Dynamic simulation code and Doublet Dynamic simulation code. This code was made available on GitHub. All codes can be downloaded at this address: https://github.com/Violaine-Gascuel/Dynamic-modeling-of-intermediate-depth-geothermal-systems-combined-with-heat-pumps (accessed on 4 May 2025).

Author Contributions: Conceptualization, V.G., J.R. and C.R.; methodology, V.G. and J.R.; software, V.G.; validation, V.G., J.R. and C.R.; formal analysis, V.G.; investigation, V.G.; resources, V.G.; data curation, V.G.; writing—original draft preparation, V.G.; writing—review and editing, V.G., J.R. and C.R.; supervision, J.R. and C.R.; project administration, J.R. and C.R.; funding acquisition, J.R. and C.R. All authors have read and agreed to the published version of the manuscript.

Funding: This research was funded through the GeoEnergy program of the Geological Survey of Canada, within the Lands and Minerals Sector of Natural Resources Canada (NRCan).

Data Availability Statement: The original contributions presented in this study are included in the article Supplementary Materials. Further inquiries can be directed to the corresponding author.

Acknowledgments: The authors would like to thank Andrew Wigston of CanmetENERGY of NRCan for his careful internal review and relevant comments. The publication would not have been possible without the help of Fiona Chapman of the Institut national de la recherche scientifique.

Conflicts of Interest: The authors declare no conflicts of interest.

Abbreviations and Symbols

The following abbreviations are used in this manuscript:

Abbreviation	**Definition**
BHE	Borehole heat exchanger
COP	Coefficient of performance
DBHE	Deep borehole heat exchanger
ELT	Entering load temperature of a heat pump (on the consumer's side)
EST	Entering source temperature of a heat pump (on the geothermal system's side)
LLT	Leaving load temperature of a heat pump (on the consumer's side)
LST	Leaving source temperature of a heat pump (on the geothermal system's side)
O&G	Oil and gas
TDS	Total dissolved solids
Tr-BR-Ch	Unit combining the Trenton, Black-River, and Chazy groups

Symbol	**Definition**	**Unit**
Coef	Coefficient	(-)
COP	Coefficient of performance of a heat pump	(-)

Cpm	Specific heat capacity	J kg^{-1} K^{-1}
Cpv	Volumetric heat capacity	J m^{-3} K^{-1}
D	Diameter	M
E	Energy	Wh
Eff	Efficiency of the heat transfer in the plate heat exchanger	(-)
EST	Entering source temperature of the heat pump (on the side of the geothermal system)	°C
F	Friction factor	(-)
G	Acceleration constant of Earth's gravity	m s^{-2}
LST	Leaving source temperature of the heat pump (on the side of the geothermal system)	°C
Power	Power	W
Q	Flow rate	m^3 s^{-1}
Q̌	Heat transfer inside the plate heat exchanger	Wtb
R	Radius	m
Re	Reynolds number	(-)
S	Tube section	m^2
t	Time	S
T	Temperature	°C
TDS	Total dissolved solids content	wt%
Utilfactor	Equivalent utilization factor at the flow rate considered	(-)
V	Velocity	m s^{-1}
A	Thermal diffusivity	m^2 s^{-1}
B	Curvature angle at the bottom of a DBHE	Rad
Δ	Rugosity	m
Δ*P*	Pressure losses	Pa
H	Efficiency of the circulation loop	(-)
P	Density	kg m^3
μ	Dynamic viscosity	Pa s^{-1}
Subscript	**Definition**	
B	Brine	
Conso	Electricity consumption	
Circu	Energy required to circulate the fluid inside the DBHE	
Gen	Energy generated by the geothermal system (ECF or doublet + heat pumps)	
Haaland	Refers to Haaland's formula	
Hp	Heat pump	
In	Inlet of the DBHE or inlet of the injection well of a doublet	
Inj	Injected brine	
Inner	Inner pipe of DBHE	
Max	Maximum	
Net	Thermal energy produced minus electricity consumed	
Out	Outlet of a DBHE or of the production well of a doublet	
Outer	Outer pipe of a DBHE	
Prod	Brine produced	
Res	Reservoir	
Singularity	Fluid flow singularity	
Static	Pressure of a column of fluid	
Tot	Total	
W	Mix of water and antifreeze circulating in the intermediate loop	

Appendix A. Code Validation

Appendix A.1. Brine Heat Capacity Function Validation

In the dynamic doublet simulation launch code, the heat capacity of the brine is calculated with the function *Cap_th_Jamieson*, based on its salinity and the average reservoir temperature.

Schröder et al. [74] developed a method to evaluate the heat capacity of geothermal waters, which was based on the heat capacity of aqueous NaCl solutions of known salinity, temperature, and pressure. To validate our function, we compared the results reported in Schröder et al. [74] with results obtained with our function (Figure A1). The difference between the values computed with our function and those measured by Schröder et al. [74] was calculated (Figure A2). The error is <1% for the tested solutions having salt concentrations < 0.15 kg kg^{-1}. It is greater for solutions with a higher salinity, with the maximum error of 2.5% for brine with 0.18 kg kg^{-1} of NaCl, a temperature of 47.4 °C and a pressure of 1 MPa.

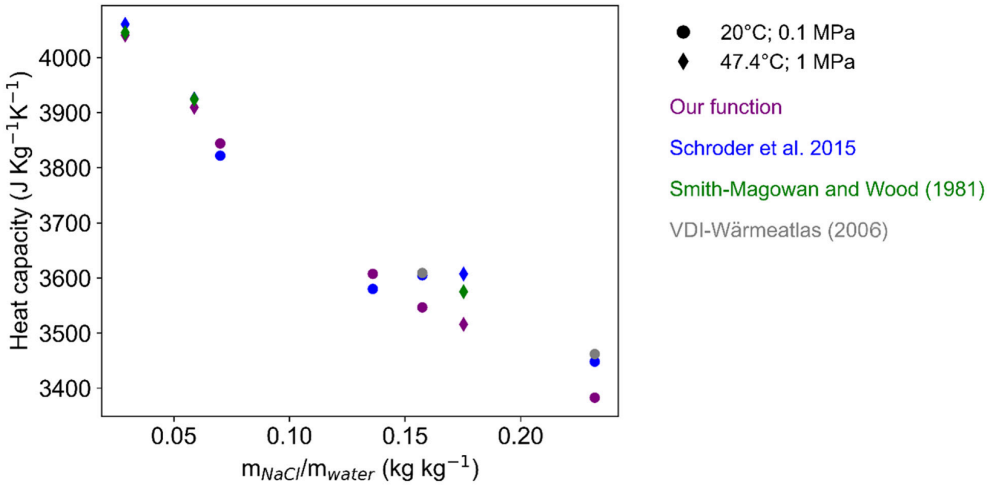

Figure A1. Heat capacities of aqueous NaCl solutions measured by Schröder et al. [74], Smith-Magowan and Wood [75] and VDI-Wärmeatlas [76] compared to the heat capacities calculated with our brine function.

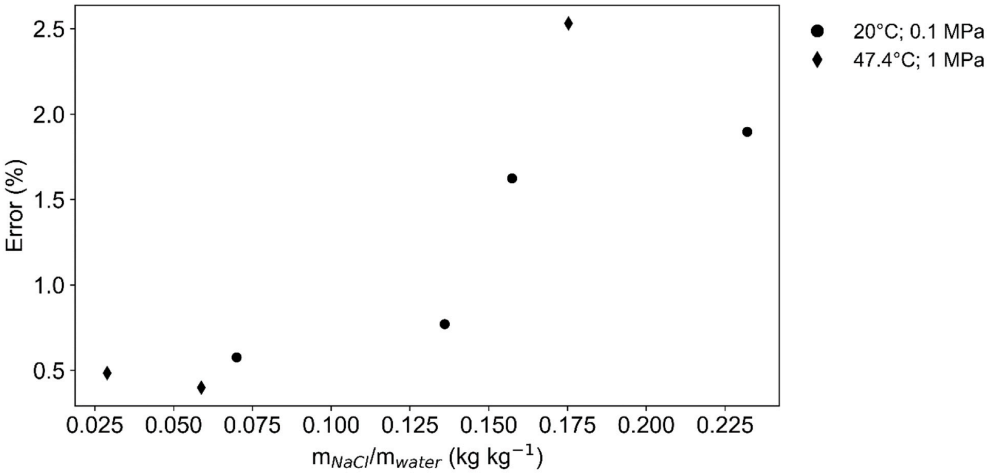

Figure A2. Error in the heat capacities calculated with our brine function when compared to the heat capacity measured by Schröder et al. [74].

Appendix A.2. Heat Loss Function Validation for a Well Doublet

The function used to calculate heat losses in the Code developed was tested against the base case of Brown and Falcone [56], who investigated wellbores with a single fluid phase (water). Brown and Falcone [56] simulated heat transfer by conduction in the production well of an open loop system using the OpenGeoSys software in their reservoir model. A dual continuum approach was used, using 1D linear elements to represent the wellbore and 3D elements to model the subsurface geology. The governing equations of Chen et al. [77] were used to simulate heat transfer within the well. Brown and Falcone [56] compared the results from this simulation with those obtained by Brown et al. [78] and the results obtained with their own method based on the work of Ramey [55].

The function Perte_Temp_remonte_Ramey included in the Code for doublet dynamic simulation was tested using parameters corresponding to the study case provided in Brown and Falcone [56] (Table A1). The inner pipe diameter was used as the production well diameter in our function.

Table A1. Parameters of the wellbore modeled in Brown et al. [78].

	Value	Unit
Borehole diameter	216	mm
Inner pipe diameter	177.8	mm
Borehole length	2000	m
Ground thermal conductivity	2.5	$W\ m^{-1}K^{-1}$
Ground heat capacity	744	$J\ kg^{-1}K^{-1}$
Water flow rate	15	$L\ s^{-1}$
Water density	980	$kg\ m^{-3}$
Water heat capacity	4178	$J\ kg^{-1}K^{-1}$
Geothermal gradient	25	$°C\ km^{-1}$
Temperature at the surface	10	°C
Inlet temperature	60	°C

As shown in Figure A3, the results from our function are in good agreement with the results of Brown and Falcone [56] when simulating long-term heat transfer. The solution based on Ramey [55] is, however, not suited to calculating heat losses over very short periods (the first few hours).

Brown and Falcone [56] also displayed the simulated temperature profile within the wellbore for different operating periods obtained with OpenGeoSys. Our function was used to calculate the outlet temperature of the production well for these time periods, and the results were compared with those of Brown and Falcone [56]. The results obtained by Brown and Falcone [56] were well reproduced for operating times of 18.5 h and longer (Figure A4). The results obtained with our function for the shortest operation time (36 min) are, however, aberrant. To avoid this problem when using this function in our code, when the operation time since the beginning of the heating season was shorter than 0.1 day (144 min), the calculation of heat losses in the production well was performed considering an operation time of 0.1 day.

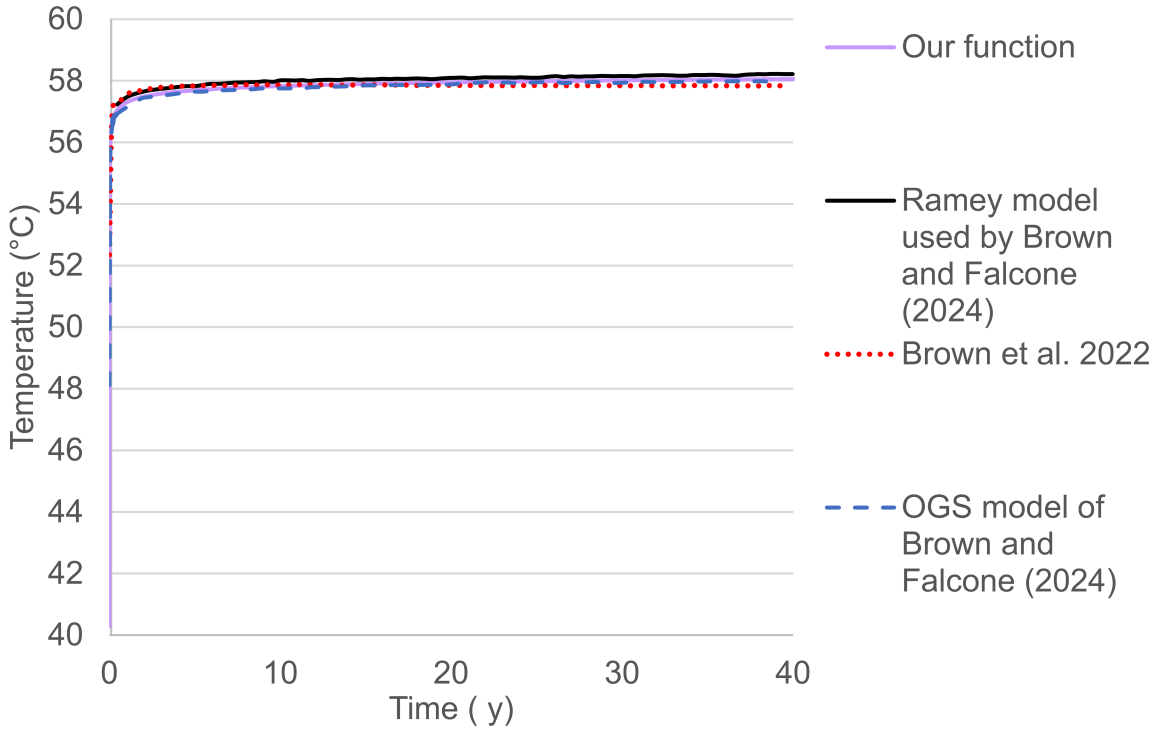

Figure A3. Comparison of the outlet temperature of the production well obtained with our heat loss function and by Brown and Falcone [56] using a solution based on Ramey [55], Brown et al. [78] and the OpenGeoSys (OGS on the figure) model of Brown and Falcone [56].

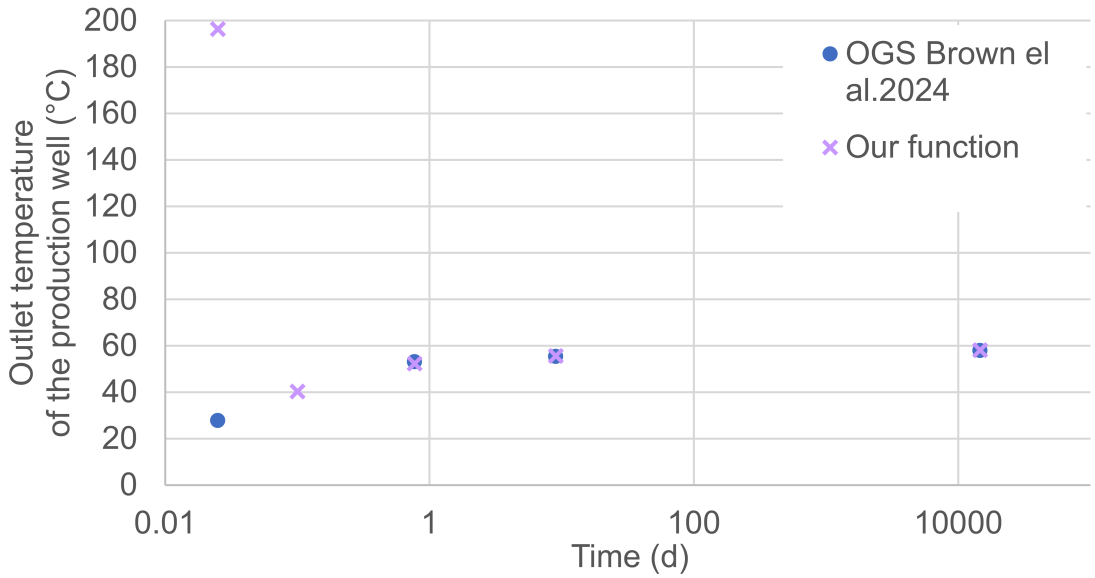

Figure A4. Comparison of the outlet temperature obtained by Brown and Falcone [56] with their OpenGeoSys (OGS on the figure) model and with our heat loss function for different operation periods. An additional data point, calculated with our function, was added for 0.1 day. The outlier estimated with our function at early times is shown for comparison purposes only, as a correction is applied to avoid aberrant results for very short operating periods.

Appendix A.3. Plate Heat Exchanger Function Validation

Our code for the dynamic simulation of geothermal doublets also includes a function to simulate the imperfect heat transfer in a plate heat exchanger, separating the brine loop from the intermediate loop in which either fresh water or a mix of water and antifreeze

circulates. This function was used to reproduce the results of Brown et al. [60], who carried out a thermal and economic analysis of heat exchangers. The properties from Brown et al. [60], the flow rates on both sides, the outlet temperature of the geothermal doublet, and the return temperature of the fluid entering the plate heat exchanger on the district heating side, as well as the heat transfer coefficient of the plate heat exchanger, were used to calculate the temperatures of the fluids exiting the plate heat exchanger on both sides. Similar to Brown et al. [60], the fluid temperatures on both sides of the plate heat exchanger were calculated for different heat transfer areas, ranging from 10 to 400 m^2.

Since our code uses the heat transfer efficiency of the plate heat exchanger as an input, it had to be calculated beforehand. Equations (A1)–(A3), taken from Brown et al. [60], were used.

$$\varepsilon = \frac{(1 - e^D)}{\left(\frac{C_h}{C_c}\right) - e^D} \tag{A1}$$

with

$$C_h = Cpv_B \times Q_B \text{ and } C_c = Cpv_w \times Q_w \tag{A2}$$

and

$$D = U \times A \times \left(\frac{1}{C_h} - \frac{1}{C_c}\right) \tag{A3}$$

with U (W m^{-2} K^{-1}) being the heat transfer coefficient and A (m^2) the heat transfer area.

Our function was able to reproduce the results of Brown et al. [60] accurately (Figures A5 and A6).

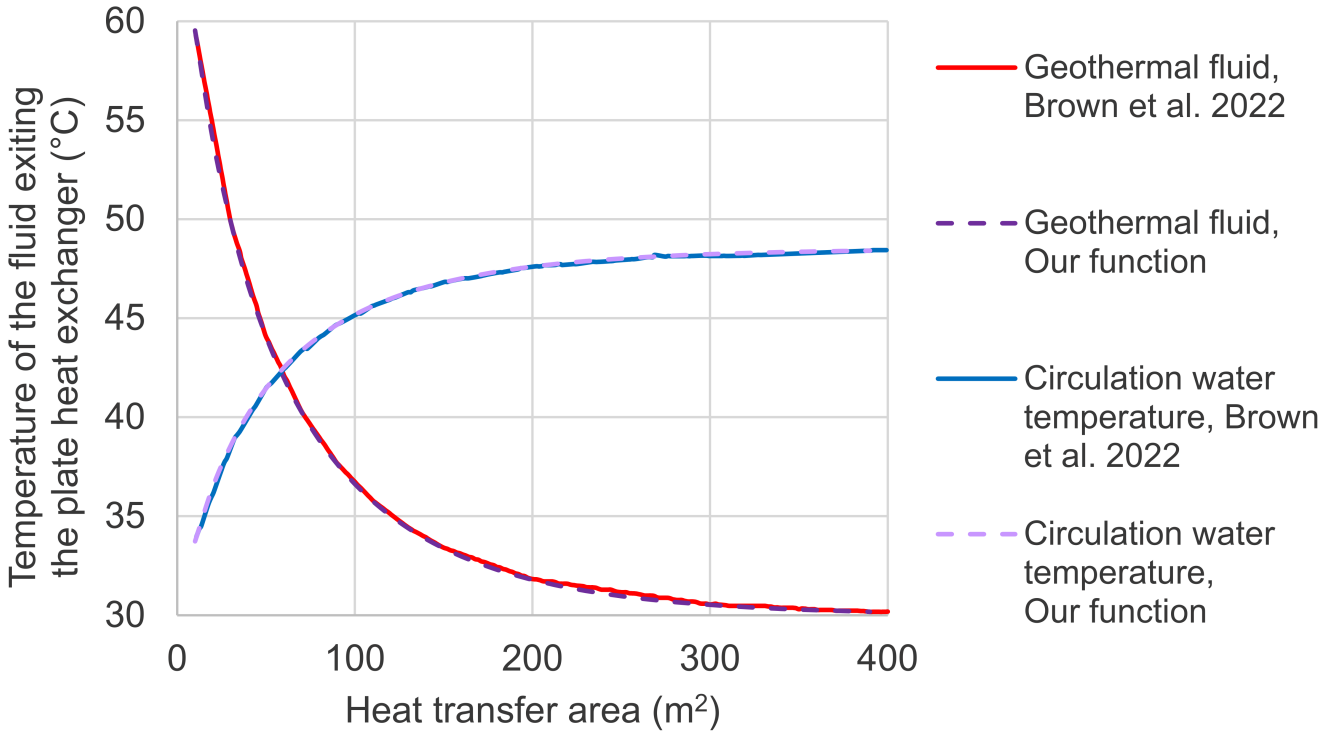

Figure A5. Comparison of the temperatures of the exiting fluids obtained on both sides of the plate heat exchanger by Brown et al. [60] and the results obtained with our plate heat exchanger function, for an inlet geothermal fluid temperature of 67 °C.

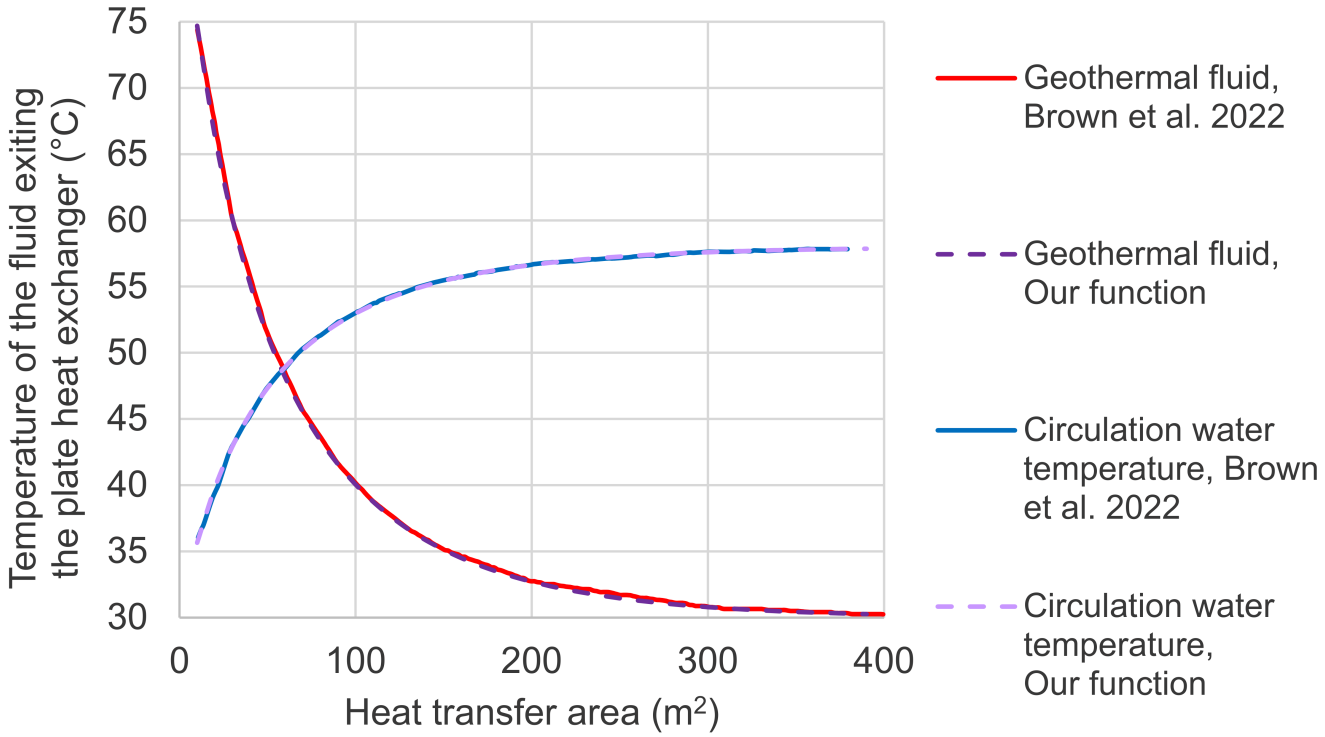

Figure A6. Comparison of the temperatures of the exiting fluids obtained on both sides of the plate heat exchanger by Brown et al. [78] and the results obtained with our plate heat exchanger function, for an inlet geothermal fluid temperature of 86 °C.

Appendix A.4. Pressure Loss Functions Validation

Functions using either the Blasius formula or the Harland formula to calculate the friction factor were developed to calculate the pressure losses due to friction in a coaxial DBHE and in the production and injection well of a geothermal doublet. The Blasius-based function assumes that the pipes are smooth, while the Haaland formula uses a user-defined pipe(s) roughness as an input. While by default the one based on the Blasius formula is used by the interpretation code, the Haaland-based function could be used by just changing which function is being called and its input parameters. Thus, both were tested against data in the literature for a coaxial DBHE and for a production well of a doublet.

Appendix A.4.1. Coaxial DBHE

The validity of the pressure loss functions for a coaxial DBHE was assessed using the base-case example of Brown et al. [56], which uses the Darcy–Weisbach equation with Petukhov's relation for the friction factor to calculate pressure losses, assuming constant fluid density and viscosity. The pressure drop, which was rounded off by Brown et al. [56], was recalculated here using the equation provided in the article for greater accuracy.

In our code, the functions used to calculate pressure losses (*perte_de_charge* and *perte_de_chargee_Haaland*, respectively using the Blasius formula and Haaland formula to calculate the friction factor) use temperature-dependent density and viscosity, computed along a temperature profile at a certain time. To better compare them with the results of Brown et al. [56], simplified versions of these functions, using user-defined constant density and viscosity, were created. Then, to test the versions of our function featuring temperature-dependent viscosities and density for the fluid, the simulated temperature profile provided in Brown et al. [56], after 25 years of operation, was used to calculate the

pressure loss at this time (Figure A7). The fluid circulating in the DBHE was considered to be pure water, similarly to Brown et al. [56]. The density and viscosity of the fluid were thus calculated along the pipes according to the temperature profile using the function eau_prop from Pr. Louis Lamarche of ÉTS (personal communication). The different functions and values of density and viscosity in the different scenarios are listed in Table A2. All scenarios consider the base-case coaxial DBHE of Brown et al. [56], an 800 m deep coaxial DBHE, having an outer pipe outer diameter of 177.9 mm and thickness of 8.1 mm, and an inner pipe outer diameter of 100.5 mm and thickness of 6.9 mm with a flow rate of 5 L s^{-1}.

Table A2. Formula used to calculate the friction factor, density and viscosity of the heat carrier fluid and phenomena taken into account in the different scenarios used to test the functions used to calculate pressure losses and the consumption of the circulation pump in coaxial DBHEs.

Scenario	Formula to Calculate the Friction Factor	Density and Viscosity	Phenomena Taken into Account
a: Brown et al. [56]	Petukhov's formula	Density: 998 kg m^{-3} Viscosity: 8×10^{-4} kg $m^{-1}s^{-1}$	Linear pressure losses along the pipes
b	Blasius' formula	Density: 998 kg m^{-3} Viscosity: 8×10^{-4} kg $m^{-1}s^{-1}$	Linear pressure losses along the pipes Pressure losses due to the change of direction and section at the bottom of the DBHE
c	Petukhov's formula	Density: 1000 kg m^{-3} Viscosity: 1.43×10^{-3} kg $m^{-1}s^{-1}$ Corresponding to the averages of the values calculated using the temperature profile	Linear pressure losses along the pipes
d: Function used by default in our code	Blasius' formula	Temperature-dependant density and viscosity calculated using the temperature profile	Linear pressure losses along the pipes Pressure losses due to the change of direction and section at the bottom of the DBHE Density driven flow
e	Haaland's formula	Temperature dependant density and viscosity calculated using the temperature profile	Linear pressure losses along the pipes Pressure losses due to the change of direction and section at the bottom of the DBHE Density-driven flow

The pressure losses obtained for these different scenarios are displayed in Figure A7. While the pressure losses obtained with our default function (scenario d) are greater than those obtained by Brown (scenario a; 96.3 MPa against 84.6 MPa), much of this difference can be attributed to the different density and viscosity values used for the heat carrier fluid. Indeed, scenarios a and b, which both used the densities and viscosity values of Brown et al. [56], yield very similar results (Figure A7; 0.99 kPa difference, corresponding to 1.2% of the pressure loss). Similar results were also obtained for scenario C, in which the formula used by Brown et al. [56] was used, taking into account the average density and viscosity calculated from the temperature profile, and our default function, which used temperature-dependent properties for the fluid (scenario D; 97.0 MPa and 96.3 MPa respectively, a 0.7% difference). A slightly lower but still similar value was obtained using the Haaland formula with a null roughness for the pipes (94.1 MPa, scenario E).

The pressure losses due to the flow singularity at the bottom of the well, which are considered in our functions but not by Brown et al. [56], were also verified to have only a minor impact. Indeed, using the simplified Blasius formula (with constant density and viscosity; scenario B), they would represent only 1.05 kPa, corresponding to 1.2% of the total pressure losses in the DBHE.

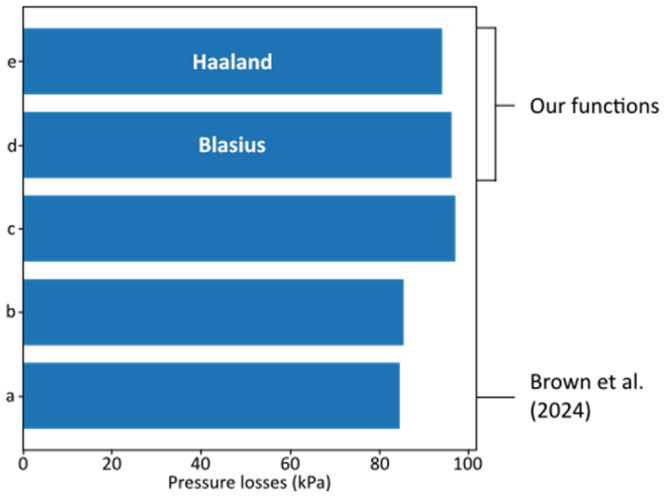

Figure A7. Pressure loss calculated with various functions for an 800 m deep coaxial DBHE, having an outer pipe outer diameter of 177.9 mm and thickness of 8.1 mm and an inner pipe outer diameter of 100.5 mm and thickness of 6.9 mm, with a flow rate of 5 L s^{-1} (base-case coaxial DBHE in Brown et al. [43]).

The power consumption of the circulation pump was calculated for the various scenarios, assuming a pump efficiency of 60% (same efficiency as in Brown et al. [56]). The same trends can be observed when looking at the calculated power consumption of the circulation pump (Figure A8).

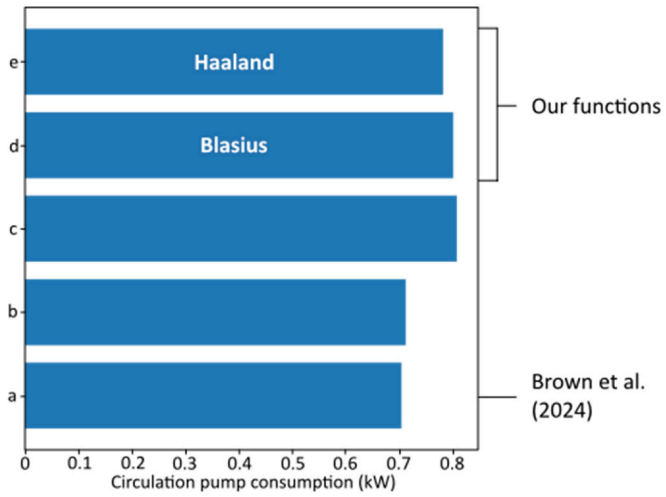

Figure A8. Power consumption of the circulation pump calculated with various functions for the pressure loss for an 800 m-deep coaxial DBHE, with an outer pipe outer diameter of 177.9 mm and thickness of 8.1 mm and an inner pipe outer diameter of 100.5 mm and thickness of 6.9 mm, with a flow rate of 5 L s^{-1} (base-case coaxial DBHE in Brown et al. [56]). The efficiency of the circulation pump is assumed to be 60%.

Appendix A.4.2. Doublet

To calculate the pressure losses due to friction in the wells of a geothermal doublet, two functions—*Head_loss_doublet* and *Head_loss_doublet_Haaland*—were developed, respectively based on the Blasius and Haaland friction factors.

These functions were validated against the results of Ricard et al. [79], in which the pressure losses in a 3000 m-deep production well were calculated for several diameters and flow rates. To calculate these pressure losses, Ricard et al. [79] used an equation based on the Moody friction factor, which takes the roughness of the pipe into account. It was assumed that Ricard et al. [79] used the density and viscosity of pure water at 20 °C. To apply our Haaland-based function, a roughness of 3.505×10^{-5} m was considered, based on Van Wees et al. [80] and Ricard et al. [79].

Both functions reproduce the results of Ricard et al. [79] fairly well for low flow rates and for the larger well diameters (Figure A9). However, for wells with a smaller diameter and higher flow rates, the roughness of the casing needs to be considered. Thus, while the results obtained with the Haaland-based function reproduce those of Ricard et al. [79] relatively well, even in these conditions, the Blasius-based function, which assumes a smooth casing, significantly underestimates the head loss (by 43% for the 6-inch casing at 220 kg s^{-1}).

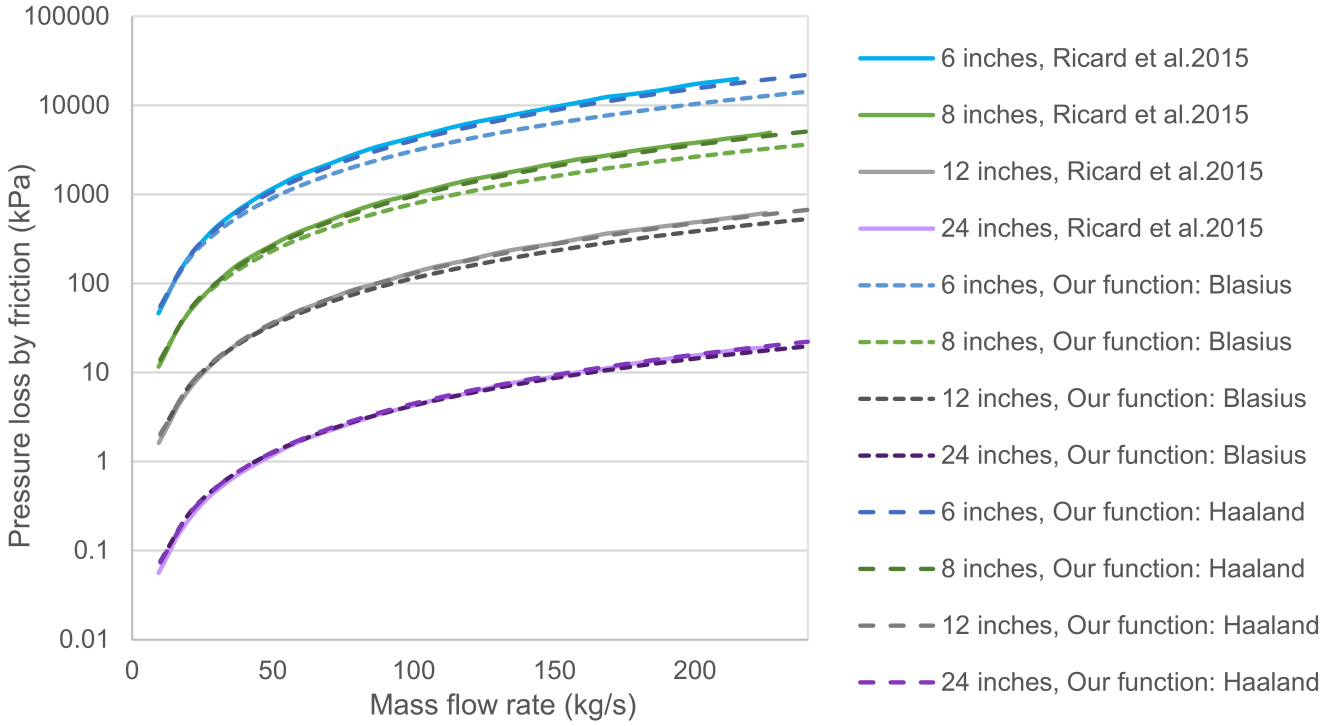

Figure A9. Pressure losses in a 3000 m-deep doublet production well, calculated for various diameters and flow rates by Ricard et al. [79] and with our functions.

The pumping power consumption due to those pressure losses caused by friction was calculated, assuming a pump efficiency of 60% (Figure A10). The same trends can be observed.

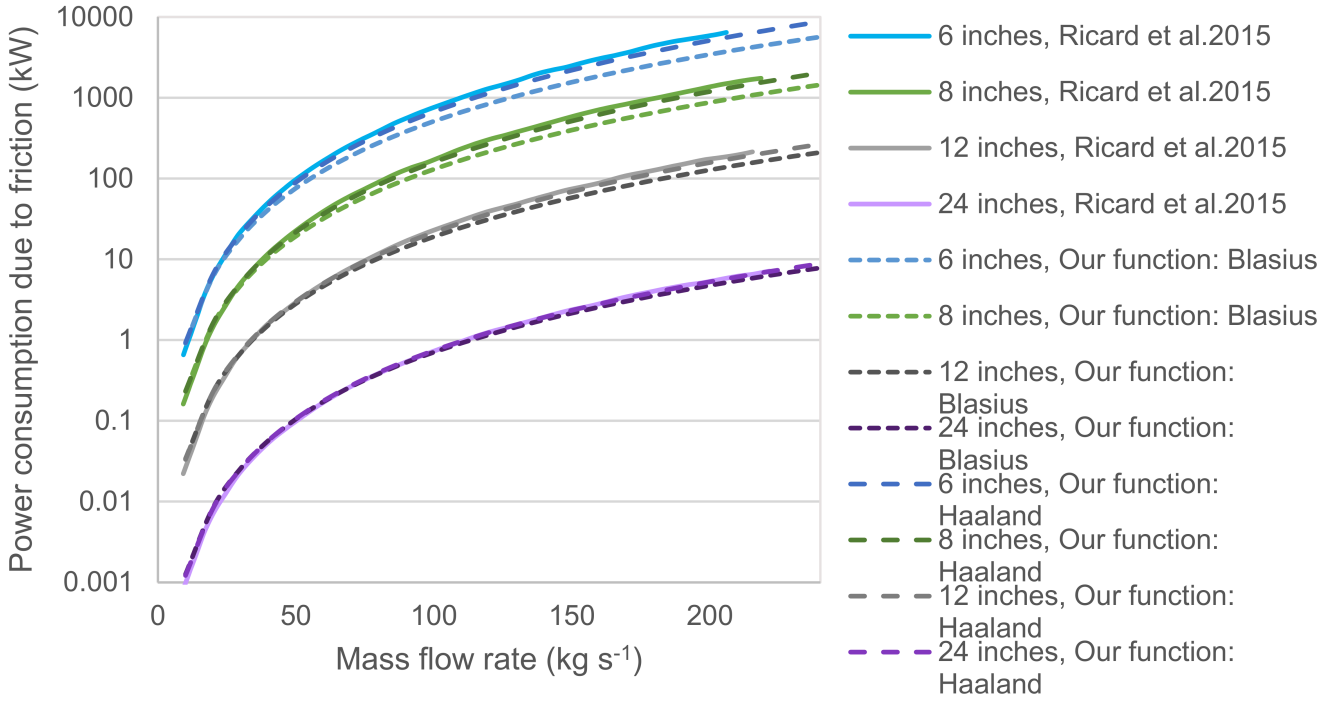

Figure A10. Pumping power due to friction in a 3000 m-deep doublet production well, calculated for various diameters and flow rates by Ricard et al. [79] and with our functions.

Appendix B. Illustrative Example

Appendix B.1. Characteristics of the Wells to Be Repurposed

Appendix B.1.1. Well A250

Well A250 was drilled in 2004 as an exploration well for a gas storage project. The well dimensions are presented in Table A3. The casing "bowl" from which depths are measured (hence the use of "KB" after the unit, representing a net length that does not account for possible deviation from the vertical) is 1.9 m above the ground surface. According to available records, the well is also equipped with an 827.7 m-long production tubing and a packer at 808.7 mKB. Traces of gas have been reported at the bottom of the Trenton and Black-River groups.

Table A3. Dimensions of well A250 based on drill reports.

Items	Bottom Depth	Diameter of the Drilling Tool	Diameter of the Casing
Units	(mKB)	(mm)	(mm)
Hole driver	4	Casing sunk	340
Borehole			
Surface	38	311	244
Intermediate	175	222	177
Open section	1048.5	156	No casing

Appendix B.1.2. Well A239

Well A239 was drilled in 2003 as a gas exploration well, targeting the Tr-BR-Ch unit and the top of the Beauharnois Formation. Pumping tests produced both brine and some natural gas.

The well dimensions are presented in Table A4. The available records indicate that this well is equipped with a 773 m-long uncemented production tubing.

Table A4. Dimensions of well A239 based on drill reports.

Items	Depth	Diameter of the Drilling Tool	Diameter of the Casing
Units	(mKB)	(mm)	(mm)
Hole driver	10	Casing sunk	356
Borehole			
Surface	121	311	219
Intermediate	786	200	140
Open section	936	121	No casing

Appendix B.2. Hydraulic and Thermal Properties of the Rocks and Brine

The thermal and hydraulic properties assigned in the models are provided in Table A5. They are similar to those used in the base-case scenario of Gascuel et al. [13], with some differences for thermal conductivity (based on well A250 instead of well A198) and refined estimates for the specific storage.

The specific storage values were calculated from porosity and compressibility values for each unit. Porosity values for Utica Tr-Br-Ch, Beauharnois, Theresa, Cairnside and Covey Hill were taken from the average porosity of well logs in Tran Ngoc et al. [66]. This type of data was not available for the Lorraine unit and Grenville basement. A porosity value measured for core from well A025 and reported in Tran Ngoc et al. [66] was used for the Lorraine unit, while the porosity in the Grenville basement was assumed to be null. The compressibility values of the aquifer matrix in the Lorraine Group, Utica Shale, Tr-Br-Ch unit, and Beauharnois and Theresa formations, and in the Grenville basement, were taken from Konstantinovskaya et al. [69], while those of the Cairnside and Covey Hill formations were taken from Tran Ngoc et al. [66]. A compressibility of 4.2×10^{-10} Pa^{-1} (compressibility of water) was used for the brine inside the pores.

The brine was considered to have a uniform TDS of 9.723 104 mg L^{-1}, corresponding to an average value based on chemical analyses performed in the Trenton Group in well A196 (1.3–1.4 km away from both wells A250 and A239). The corresponding average density of 1063 kg m^{-3} and a viscosity of 1.74 10^3 Pa s, calculated using the expression of Phillips [81] presented in Adams and Bachu [82] and considering NaCl only (i.e., the dominant compound), were used in the model.

In the doublet numerical model, temperature-dependent brine density (nonlinear) and viscosity were considered. They were expressed with Equations (A4)–(A6), with a density formula, as already implemented in FEFLOW, based on Perrochet [83]. According to Diersch and Kolditz [84], this formula accurately matches the fluid density over a wide range of temperatures and accounts for the density anomaly at 4 °C.

$$\rho_B(T) = a + bT + cT^2 + dT^3 + eT^4 + fT^5 + gT^6 \quad \text{(A4)}$$

with a = 9.998396×10^2, b = 6.764771×10^{-2}, c = -8.993699×10^{-3}, d = 9.143518×10^{-5}, e = -8.907391×10^{-7}, f = 5.291959×10^{-9} and g = $-1.359813 \times 10^{-11}$. The density is in kg m^{-3} (or g L^{-1}).

The formula used in FEFLOW for relative fluid viscosity is

$$\frac{\mu}{\mu_{Ref}} = \frac{1 + 0.7063 \times \tau_{Ref} - 0.04832 \times \tau_{Ref}^3}{1 + 0.7063 \times \tau - 0.04832 \times \tau^3} \quad \text{(A5)}$$

with

$$\tau = \frac{T - 150}{100} \text{ and } \tau_{Ref} = \frac{T_{\text{Ref}} - 150}{100} \quad \text{(A6)}$$

Table A5. Hydraulic and thermal properties of the rock units.

Units	Depth of Bottom	Hydraulic Properties				Thermal Properties	
		Hydraulic Conductivity	Porosity	Matrix Compressibility	Specific Storage	Thermal Conductivity	Volumetric Heat Capacity
	(m)	(m s^{-1})	(%)	(Pa^{-1})	(m^{-1})	(W $m^{-1}K^{-1}$)	(MJ $m^{-3}K^{-1}$)
Lorraine	620	2.39×10^{-12}	3.9	1.86×10^{-9}	1.96×10^{-5}	2.00	2.39
Utica	738	5.99×10^{-13}	4.0	1.86×10^{-9}	1.96×10^{-5}	2.15	2.28
Tr-Br-Ch	893	1.00×10^{-7}	2.2	1.86×10^{-9}	1.95×10^{-5}	2.96	2.29
Beauharnois	950	9.88×10^{-9}	1.8	1.86×10^{-9}	1.95×10^{-5}	4.27	2.33
Theresa	986	1.31×10^{-8}	4.0	1.86×10^{-9}	1.96×10^{-5}	3.35	2.31
Cairnside	1098	5.32×10^{-8}	3.3	3.96×10^{-9}	4.14×10^{-5}	4.34	2.13
Covey Hill	1358	5.33×10^{-9}	6.0	1.94×10^{-9}	2.05×10^{-5}	3.11	1.96
Socle		1.00×10^{-10}	0.0	1.81×10^{-9}	1.89×10^{-5}	2.75	1.98

Appendix B.3. Meshes Used in the Numerical Models and Verification of the Independence of the Mesh

The impact of mesh refinement was tested for each model. The meshes used were structured 3D meshes with horizontal slices. First, a horizontal mesh was created using triangular elements. For both the DBHE and the doublet, the mesh was refined around the wells using the direct estimation of the optimum nodal distance method detailed in Diersch et al. [85] to calculate the ideal distance for the six neighbor nodes. Then, several horizontal layers were added with varying thicknesses. The impact of the vertical refinement along the DBHE or the open section of the doublet's wells was assessed.

The mesh was refined further at the top and bottom of the DBHE or around both ends of the open section of the doublet's wells, where greater variations in hydraulic head and temperature are expected to occur.

To shorten the computation time, the variation in brine viscosity with temperature was neglected when running tests for the mesh independence, while the variation in density was considered to be linear.

Appendix B.3.1. DBHE

The final mesh used in the simulations comprised 109,552 elements and 41 layers, with an average layer thickness of 36.2 m along the DBHE length. The selected mesh was refined vertically down to 1 m near the top and bottom of the DBHE. The sensitivity of the outlet temperature to vertical refinement was tested, using the annular inlet configuration (i.e., the fluid was injected into the space between the pipes and flowed up through the inner pipe), with a constant injection temperature of −5 °C, a fluid flow rate of 3.03 L s^{-1} and a simulation time of 212 days (Figure A11). The selected mesh (shown in Figure A12) was considered a good compromise between accuracy and computation time.

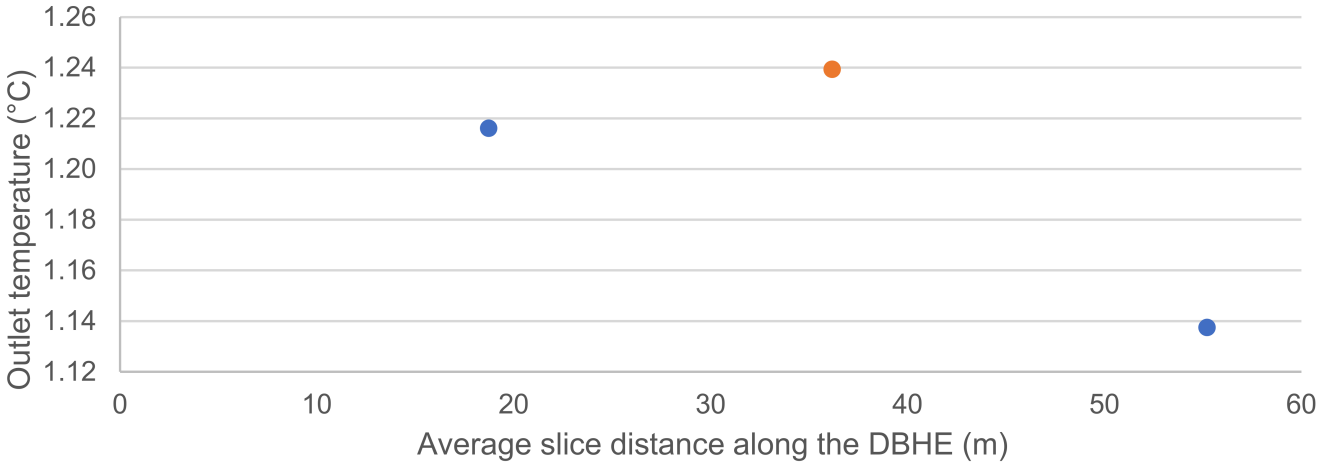

Figure A11. Sensitivity to the vertical refinement of the DBHE. The outlet temperature on this graph was simulated after 212 days for a constant injection temperature of −5 °C and a fluid flow rate of 3.03 L s^{-1}. The result corresponding to the final (selected) mesh is displayed in red, and two other meshes more and less vertically refined are shown in blue.

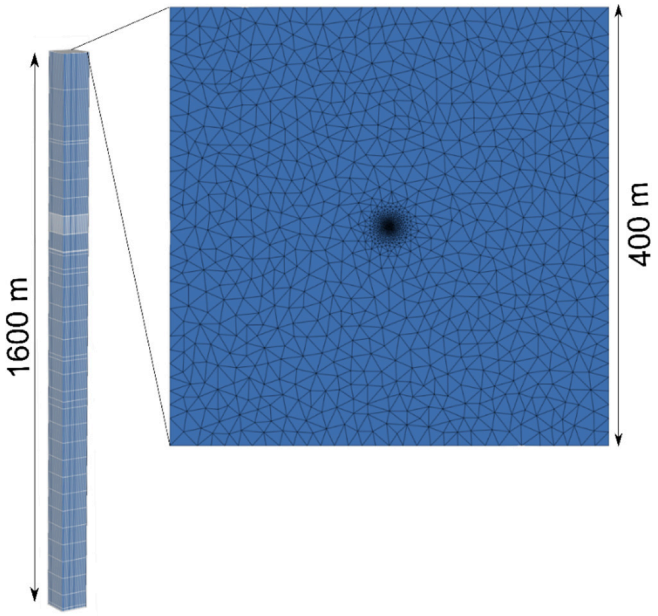

Figure A12. Mesh selected for the DBHE model.

Appendix B.3.2. Doublet

As the radius of influence of a geothermal doublet is larger than that of a DBHE, the geological units could not be considered horizontal. Elevations of the different units north of the Yamaska Fault were taken from the geological model of Claprood et al. [68]. However, as shown in Figure A13, the geological model of Claprood et al. [68] does not cover the entire FEFLOW model area. A few data points corresponding to the boundaries of the units identified in wells north of the geological model were thus added to the elevation layers to define the FEFLOW model layers. The elevations were then interpolated using data points extracted from the northern block (only) of the geological model, and additional data points using the inverse distance method with four neighbors (Figure A14). A minimum distance of 1 m was imposed between slices to avoid numerical errors. Therefore, elevations in the FEFLOW model are considered accurate within the area covered by the geological model (which includes the region around wells A250 and A239), but less accurate outside this area.

The Yamaska and Deschambault faults were considered to be no-flow boundaries. Lateral boundaries perpendicular to these faults were used to delineate the model and assigned the same constant hydraulic head boundary condition (100 m), given that groundwater flow at depth is almost null. The model extends to a depth of 2000 m into the Grenville basement. It was verified that the hydraulic head and thermal perturbation do not reach the lateral boundaries or the bottom of the model, although the hydraulic head perturbation does reach the Yamaska fault.

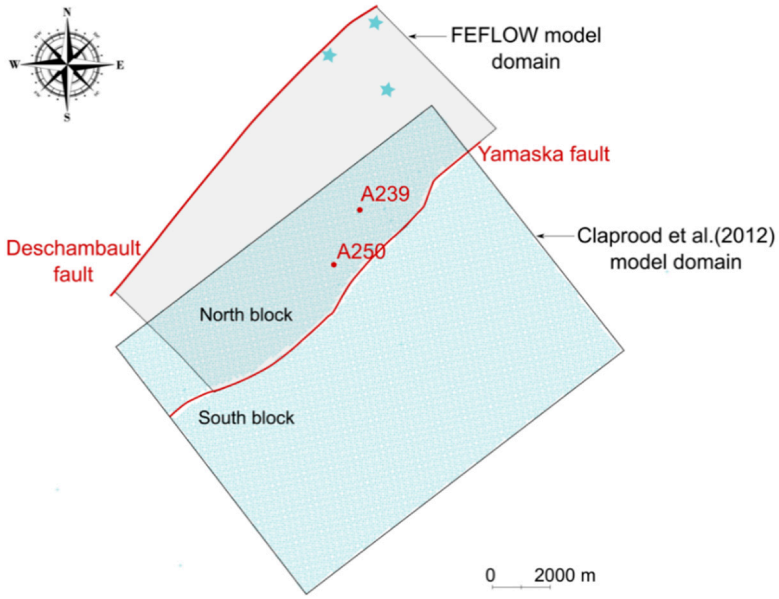

Figure A13. Delineations of the FEFLOW model and geological model. Blue crosses represent elevations extracted from the geological model of Claprood et al. [68] and blue stars denote additional data from well logs. The red dots correspond to the locations of the production (A250) and extraction (A239) wells of the modeled doublet.

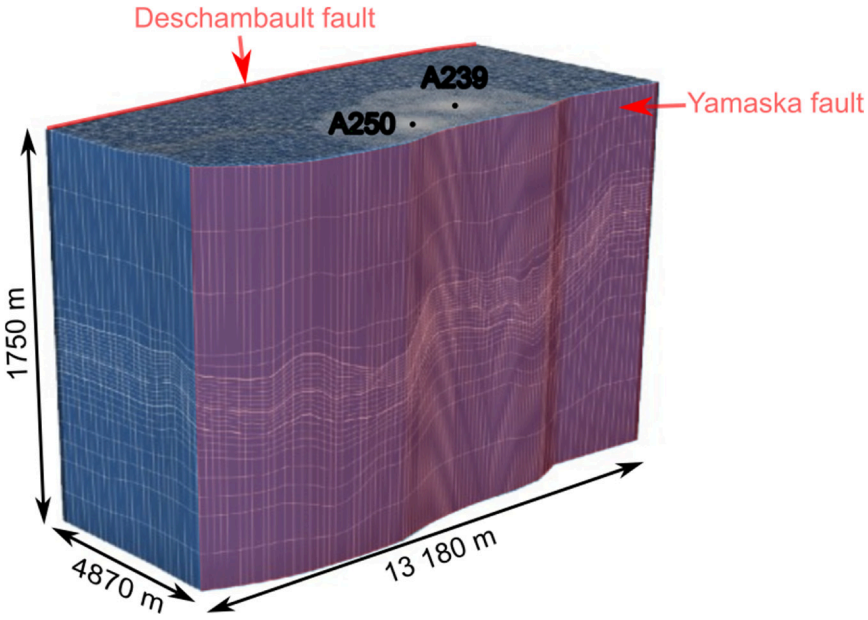

Figure A14. Mesh selected for the doublet model.

The mesh is created using tetrahedral elements. It is refined in the horizontal plane around the wells, using the direct estimation of the optimal nodal method described in Diersch et al. [85] to calculate the optimal distance of neighboring nodes. Then, the

sensitivity of the outlet temperature to vertical refinement was tested, using the selected configuration/design and constant injection temperature, fluid flow and simulation period, to make sure the final mesh is optimal for the context.

The final mesh selected comprises 462,560 elements and 33 slices. The average distance between slices is 17.3 m in the Tr-Br-Ch unit and 14.5 m in the Beauharnois Formation, with a minimum slice spacing of 1 m near the top and bottom of the open well sections. Figures A15–A17 compare the temperature at the bottom of the production well, injection head and production head simulated with the chosen mesh, after 30 years of operation, with results obtained with more or less vertically refined meshes. The chosen mesh is considered a good compromise between accuracy and calculation time (the simulation with the more refined mesh took nearly 5 h).

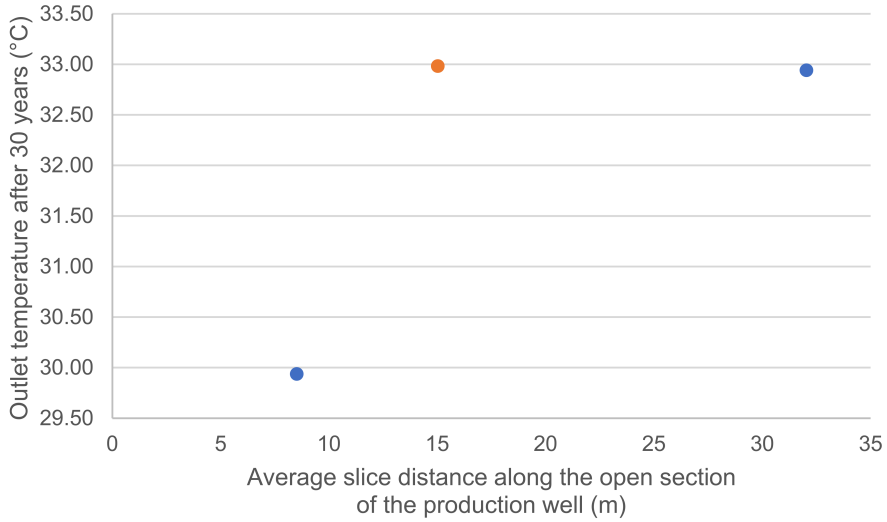

Figure A15. Sensitivity of the outlet temperature of the doublet to vertical refinement. The outlet temperature on this graph was simulated after 10,950 days for a constant injection temperature of −10 °C and a fluid flow rate of 3 L s^{-1}. The result corresponding to the final (selected) mesh is displayed in red, and two other meshes more and less vertically refined are shown in blue.

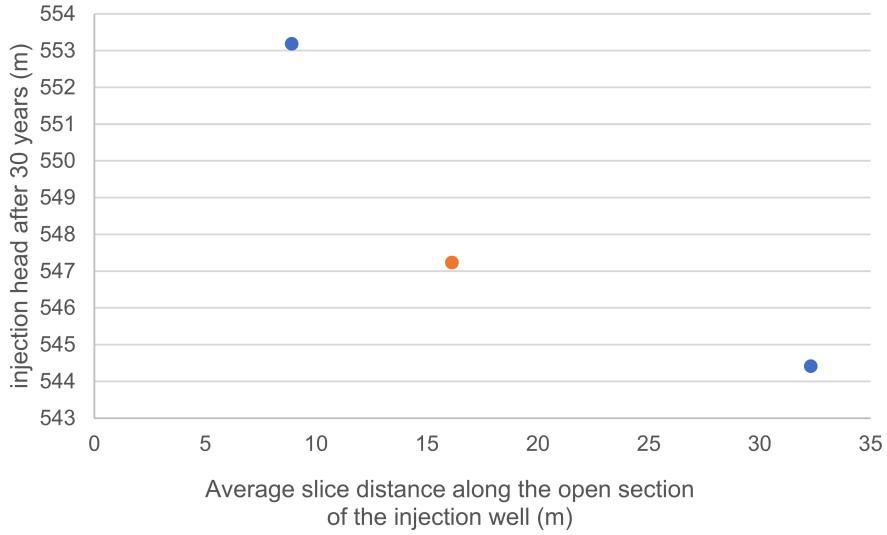

Figure A16. Sensitivity of the injection head of the doublet to vertical refinement. The injection head on this graph was simulated after 10,950 days for a constant injection temperature of −10 °C and a fluid flow rate of 3 L s^{-1}. The result corresponding to the final (selected) mesh is displayed in red and two other meshes more and less vertically refined are shown in blue.

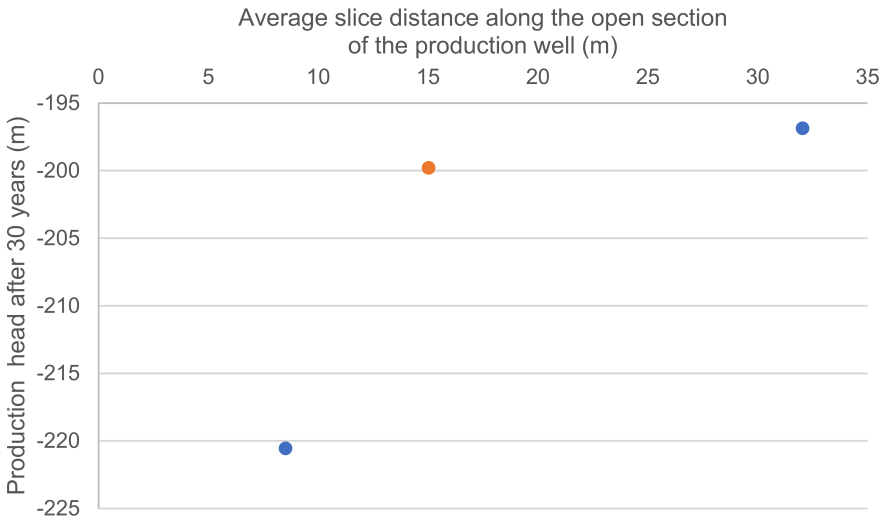

Figure A17. Sensitivity of the production head of the doublet to vertical refinement. The production head on this graph was simulated after 10,950 days for a constant injection temperature of −10 °C and a fluid flow rate of 3 L s^{-1}. The result corresponding to the final (selected) mesh is displayed in red and two other meshes more and less vertically refined are shown in blue.

References

1. Lund, J.W.; Toth, A.N. Direct utilization of geothermal energy 2020 worldwide review. *Geothermics* **2021**, *90*, 101915. [CrossRef]
2. Herreras Martínez, S.; Harmsen, R.; Menkveld, M.; Faaij, A.; Kramer, G.J. Municipalities as key actors in the heat transition to decarbonise buildings: Experiences from local planning and implementation in a learning context. *Energy Policy* **2022**, *169*, 113169. [CrossRef]
3. Xia, Z.H.; Jia, G.S.; Ma, Z.D.; Wang, J.W.; Zhang, Y.P.; Jin, L.W. Analysis of economy, thermal efficiency and environmental impact of geothermal heating system based on life cycle assessments. *Appl. Energy* **2021**, *303*, 117671. [CrossRef]
4. David, A.; Mathiesen, B.V.; Averfalk, H.; Werner, S.; Lund, H. Heat Roadmap Europe: Large-Scale Electric Heat Pumps in District Heating Systems. *Energies* **2017**, *10*, 578. [CrossRef]
5. Franco, A.; Vaccaro, M. Numerical simulation of geothermal reservoirs for the sustainable design of energy plants: A review. *Renew. Sustain. Energy Rev.* **2014**, *30*, 987–1002. [CrossRef]
6. Gascuel, V.; Raymond, J.; Rivard, C.; Marcil, J.-S.; Comeau, F.-A. Design and optimization of deep coaxial borehole heat exchangers for cold sedimentary basins. *Geothermics* **2022**, *105*, 102504. [CrossRef]
7. Kurnia, J.C.; Shatri, M.S.; Putra, Z.A.; Zaini, J.; Caesarendra, W.; Sasmito, A.P. Geothermal energy extraction using abandoned oil and gas wells: Techno-economic and policy review. *Int. J. Energy Res.* **2022**, *46*, 28–60. [CrossRef]
8. Nian, Y.-L.; Cheng, W.-L. Evaluation of geothermal heating from abandoned oil wells. *Energy* **2018**, *142*, 592–607. [CrossRef]
9. Babaei, M.; Nick, H.M. Performance of low-enthalpy geothermal systems: Interplay of spatially correlated heterogeneity and well-doublet spacings. *Appl. Energy* **2019**, *253*, 113569. [CrossRef]
10. Willems, C.J.L.; Nick, H.M.; Weltje, G.J.; Bruhn, D.F. An evaluation of interferences in heat production from low enthalpy geothermal doublets systems. *Energy* **2017**, *135*, 500–512. [CrossRef]
11. Wang, Y.; Voskov, D.; Khait, M.; Saeid, S.; Bruhn, D. Influential factors on the development of a low-enthalpy geothermal reservoir: A sensitivity study of a realistic field. *Renew. Energy* **2021**, *179*, 641–651. [CrossRef]
12. Hamm, V.; Bouzit, M.; Lopez, S. Assessment of complex well architecture performance for geothermal exploitation of the Paris basin: A modeling and economic analysis. *Geothermics* **2016**, *64*, 300–313. [CrossRef]
13. Gascuel, V.; Rivard, C.; Raymond, J. Deep geothermal doublets versus deep borehole heat exchangers: A comparative study for cold sedimentary basins. *Appl. Energy* **2024**, *361*, 122826. [CrossRef]
14. Daniilidis, A.; Nick, H.M.; Bruhn, D.F. Interdependencies between physical, design and operational parameters for direct use geothermal heat in faulted hydrothermal reservoirs. *Geothermics* **2020**, *86*, 101806. [CrossRef]
15. Ezekiel, J.; Ebigbo, A.; Arifianto, I.; Daniilidis, A.; Finkbeiner, T.; Mai, P.M. Techno-economic performance optimization of hydrothermal doublet systems: Application to the Al Wajh basin, Western Saudi Arabia. *Geothermics* **2022**, *105*, 102532. [CrossRef]
16. Brown, C.S.; Cassidy, N.J.; Egan, S.S.; Griffiths, D. Numerical modelling of deep coaxial borehole heat exchangers in the Cheshire Basin, UK. *Comput. Geosci.* **2021**, *152*, 104752. [CrossRef]
17. Dijkshoorn, L.; Speer, S.; Pechnig, R. Measurements and design calculations for a deep coaxial borehole heat exchanger in Aachen, Germany. *Int. J. Geophys.* **2013**, *2013*, 916541. [CrossRef]

18. Schincariol, R.A.; Raymond, J. Borehole Heat Exchangers—Addressing the Application Gap with Groundwater Science. *Groundwater* **2023**, *61*, 163–170. [CrossRef] [PubMed]
19. Deng, J.; Wei, Q.; He, S.; Liang, M.; Zhang, H. Simulation Analysis on the Heat Performance of Deep Borehole Heat Exchangers in Medium-Depth Geothermal Heat Pump Systems. *Energies* **2020**, *13*, 754. [CrossRef]
20. Cai, W.; Wang, F.; Liu, J.; Wang, Z.; Ma, Z. Experimental and numerical investigation of heat transfer performance and sustainability of deep borehole heat exchangers coupled with ground source heat pump systems. *Appl. Therm. Eng.* **2019**, *149*, 975–986. [CrossRef]
21. Casasso, A.; Sethi, R. Modelling thermal recycling occurring in groundwater heat pumps (GWHPs). *Renew. Energy* **2015**, *77*, 86–93. [CrossRef]
22. Liu, J.; Wang, F.; Gao, Y.; Zhang, Y.; Cai, W.; Wang, M.; Wang, Z. Influencing factors analysis and operation optimization for the long-term performance of medium-deep borehole heat exchanger coupled ground source heat pump system. *Energy Build.* **2020**, *226*, 110385. [CrossRef]
23. Xu, T.; Hu, Z.; Feng, B.; Feng, G.; Li, F.; Jiang, Z. Numerical evaluation of building heating potential from a co-axial closed-loop geothermal system using wellbore–reservoir coupling numerical model. *Energy Explor. Exploit.* **2020**, *38*, 733–754. [CrossRef]
24. Biglarian, H.; Abbaspour, M.; Saidi, M.H. Evaluation of a transient borehole heat exchanger model in dynamic simulation of a ground source heat pump system. *Energy* **2018**, *147*, 81–93. [CrossRef]
25. Natale, C.; Naldi, C.; Dongellini, M.; Morini, G.L. Dynamic modelling of a dual-source heat pump system through a Simulink tool. *J. Phys. Conf. Ser.* **2022**, *2385*, 012090. [CrossRef]
26. Ballerini, V.; Rossi di Schio, E.; Valdiserri, P.; Naldi, C.; Dongellini, M. A Long-Term Dynamic Analysis of Heat Pumps Coupled to Ground Heated by Solar Collectors. *Appl. Sci.* **2023**, *13*, 7651. [CrossRef]
27. Zhao, P.; Zhang, D.; Li, X.; Gao, P.; Lin, Y.; Chu, Z. Dynamic numerical investigation of the long-term performance of a GSHP system considering groundwater seepage and layered subsurface coupling conditions. *Appl. Therm. Eng.* **2023**, *222*, 119944. [CrossRef]
28. Hein, P.; Kolditz, O.; Görke, U.-J.; Bucher, A.; Shao, H. A numerical study on the sustainability and efficiency of borehole heat exchanger coupled ground source heat pump systems. *Appl. Therm. Eng.* **2016**, *100*, 421–433. [CrossRef]
29. Zanetti, E.; Bonduà, S.; Bortolin, S.; Bortolotti, V.; Azzolin, M.; Tinti, F. Sequential coupled numerical simulations of an air/ground-source heat pump: Validation of the model and results of yearly simulations. *Energy Build.* **2022**, *277*, 112540. [CrossRef]
30. Boban, L.; Soldo, V.; Fujii, H. Investigation of heat pump performance in heterogeneous ground. *Energy Convers. Manag.* **2020**, *211*, 112736. [CrossRef]
31. Li, W.; Li, X.; Wang, Y.; Tu, J. An integrated predictive model of the long-term performance of ground source heat pump (GSHP) systems. *Energy Build.* **2018**, *159*, 309–318. [CrossRef]
32. Zhang, X. Numerical study of geothermal district heating from a ground heat exchanger coupled with a heat pump system. *Appl. Therm. Eng.* **2021**, *185*, 116335. [CrossRef]
33. Wang, Z.; Wang, F.; Liu, J.; Li, Y.; Wang, M.; Luo, Y.; Ma, L.; Zhu, C.; Cai, W. Energy analysis and performance assessment of a hybrid deep borehole heat exchanger heating system with direct heating and coupled heat pump approaches. *Energy Convers. Manag.* **2023**, *276*, 116484. [CrossRef]
34. Wang, X.; Su, Y.; Liu, G.; Ni, L. Numerical investigation of the deep borehole heat exchanger in medium-depth geothermal heat pump system for building space heating. *Energy Build.* **2024**, *304*, 113874. [CrossRef]
35. Thomasson, T.; Abdurafikov, R. Dynamic simulation and techno-economic optimization of deep coaxial borehole heat exchangers in a building energy system. *Energy Build.* **2022**, *275*, 112457. [CrossRef]
36. Luo, Y.; Xu, G.; Zhang, S.; Cheng, N.; Tian, Z.; Yu, J. Heat extraction and recovery of deep borehole heat exchanger: Negotiating with intermittent operation mode under complex geological conditions. *Energy* **2021**, *241*, 122510. [CrossRef]
37. Wang, Y.; Wang, Y.; You, S.; Zheng, X.; Wei, S. Operation optimization of the coaxial deep borehole heat exchanger coupled with ground source heat pump for building heating. *Appl. Therm. Eng.* **2022**, *213*, 118656. [CrossRef]
38. Zarrella, A.; Emmi, G.; De Carli, M. A simulation-based analysis of variable flow pumping in ground source heat pump systems with different types of borehole heat exchangers: A case study. *Energy Convers. Manag.* **2017**, *131*, 135–150. [CrossRef]
39. Hu, P.; Hu, Q.; Lin, Y.; Yang, W.; Xing, L. Energy and exergy analysis of a ground source heat pump system for a public building in Wuhan, China under different control strategies. *Energy Build.* **2017**, *152*, 301–312. [CrossRef]
40. Baquedano, C.; García-Gil, A.; Marazuela, M.Á.; Carnicer, A.M.; Aguilera, H.; Santamarta, J.C.; Mejías Fernández, A. The efficiency loss in groundwater heat pump systems triggered by thermal recycling. *Renew. Energy* **2022**, *200*, 1458–1468. [CrossRef]
41. Beaudry, G.; Pasquier, P.; Marcotte, D.; Zarrella, A. Flow rate control in standing column wells: A flexible solution for reducing the energy use and peak power demand of the built environment. *Appl. Energy* **2022**, *313*, 118774. [CrossRef]
42. Tonellato, G.; Kummert, M.; Candanedo, J.A.; Beaudry, G.; Pasquier, P. A control strategy evaluation framework for ground source heat pumps using standing column wells. In *Proceedings of the IGSHPA Conference, Las Vegas, USA, 6–8 December 2022*; International Ground Source Heat Pump Association: Springfield, IL, USA, 2022; 10p.

43. Brown, C.S.; Kolo, I.; Banks, D.; Falcone, G. Comparison of the thermal and hydraulic performance of single U-tube, double U-tube and coaxial medium-to-deep borehole heat exchangers. *Geothermics* **2024**, *117*, 102888. [CrossRef]
44. Kalmár, L.; Medgyes, T.; Szanyi, J. Specifying boundary conditions for economical closed loop deep geothermal heat production. *Energy* **2020**, *196*, 117068. [CrossRef]
45. Holmberg, H.; Acuña, J.; Næss, E.; Sønju, O.K. Thermal evaluation of coaxial deep borehole heat exchangers. *Renew. Energy* **2016**, *97*, 65–76. [CrossRef]
46. Sapinska-Sliwa, A.; Rosen, M.A.; Gonet, A.; Sliwa, T. Deep borehole heat exchangers—A conceptual and comparative review. In *Proceedings of the World Geothermal Congress 2015, Melbourne, Australia, 19–25 April 2015*; International Geothermal Association: Bochum, Germany, 2015; 11p.
47. Holmslykke, H.D.; Kjøller, C.; Fabricius, I.L. Injection of Ca-depleted formation water in the Lower Triassic Bunter Sandstone Formation for seasonal heat storage in geothermal sandstone reservoirs: Effects on reservoir quality. *Geothermics* **2021**, *96*, 102179. [CrossRef]
48. Réveillère, A.; Hamm, V.; Lesueur, H.; Cordier, E.; Goblet, P. Geothermal contribution to the energy mix of a heating network when using Aquifer Thermal Energy Storage: Modeling and application to the Paris basin. *Geothermics* **2013**, *47*, 69–79. [CrossRef]
49. Diersch, H.J.G.; Bauer, D.; Heidemann, W.; Rühaak, W.; Schätzl, P. Finite element modeling of borehole heat exchanger systems: Part 1. Fundamentals. *Comput. Geosci.* **2011**, *37*, 1122–1135. [CrossRef]
50. Nian, Y.-L.; Cheng, W.-L.; Yang, X.-Y.; Xie, K. Simulation of a novel deep ground source heat pump system using abandoned oil wells with coaxial BHE. *Int. J. Heat Mass Transf.* **2019**, *137*, 400–412. [CrossRef]
51. Hu, X.; Banks, J.; Wu, L.; Liu, W.V. Numerical modeling of a coaxial borehole heat exchanger to exploit geothermal energy from abandoned petroleum wells in Hinton, Alberta. *Renew. Energy* **2020**, *148*, 1110–1123. [CrossRef]
52. Korzani, M.G.; Held, S.; Kohl, T. Numerical based filtering concept for feasibility evaluation and reservoir performance enhancement of hydrothermal doublet systems. *J. Pet. Sci. Eng.* **2020**, *190*, 106803. [CrossRef]
53. Tilley, B.S.; Baumann, T. On temperature attenuation in staged open-loop wells. *Renew. Energy* **2012**, *48*, 416–423. [CrossRef]
54. Beckers, K.F.; McCabe, K. GEOPHIRES v2.0: Updated geothermal techno-economic simulation tool. *Geotherm. Energy* **2019**, *7*, 5. [CrossRef]
55. Ramey, H.J., Jr. Wellbore Heat Transmission. *J. Pet. Technol.* **1962**, *14*, 427–435. [CrossRef]
56. Brown, C.S.; Falcone, G. Investigating heat transmission in a wellbore for Low-Temperature, Open-Loop geothermal systems. *Therm. Sci. Eng. Prog.* **2024**, *48*, 102352. [CrossRef]
57. ASHRAE. *Handbook—Fundamentals*, SI ed.; ASHRAE: Atlanta, GA, USA, 2005; Chapter 21.
58. Jamieson, D.T.; Tudhope, J.S.; Morris, R.; Cartwright, G. Physical properties of sea water solutions: Heat capacity. *Desalination* **1969**, *7*, 23–30. [CrossRef]
59. Nayar, K.G.; Sharqawy, M.H.; Banchik, L.D.; Lienhard, J.H. Thermophysical properties of seawater: A review and new correlations that include pressure dependence. *Desalination* **2016**, *390*, 1–24. [CrossRef]
60. Brown, C.S.; Cassidy, N.J.; Egan, S.S.; Griffiths, D. Thermal and Economic Analysis of Heat Exchangers as Part of a Geothermal District Heating Scheme in the Cheshire Basin, UK. *Energies* **2022**, *15*, 1983. [CrossRef]
61. Sezer, T.; Sani, A.K.; Singh, R.M.; Cui, L.; Boon, D.P.; Woods, M. Numerical investigation of a district scale groundwater heat pump system: A case study from Colchester, UK. *Appl. Therm. Eng.* **2024**, *236*, 121915. [CrossRef]
62. Daniilidis, A.; Alpsoy, B.; Herber, R. Impact of technical and economic uncertainties on the economic performance of a deep geothermal heat system. *Renew. Energy* **2017**, *114*, 805–816. [CrossRef]
63. Semple, L.; Carriveau, R.; Ting, D.S.-K. Assessing heating and cooling demands of closed greenhouse systems in a cold climate. *Int. J. Energy Res.* **2017**, *41*, 1903–1913. [CrossRef]
64. Geosmart Energy. *Specification Catalogue for Premium HT Series Hydronic System*; Geosmart Energy: Cambridge, ON, Canada, 2021; p. 54.
65. Huang, Y.; Zhang, Y.; Xie, Y.; Zhang, Y.; Gao, X. Thermal performance analysis on the composition attributes of deep coaxial borehole heat exchanger for building heating. *Energy Build.* **2020**, *221*, 110019. [CrossRef]
66. Tran Ngoc, T.D.; Lefebvre, R.; Konstantinovskaya, E.; Malo, M. Characterization of deep saline aquifers in the Bécancour area, St. Lawrence Lowlands, Québec, Canada: Implications for CO_2 geological storage. *Environ. Earth Sci.* **2014**, *72*, 119–146. [CrossRef]
67. Gascuel, V.; Raymond, J.; Rivard, C. Dynamic modeling of intermediate depth geothermal systems. In *Proceedings of IGSHPA 2024, Montréal, Canada, 28–30 May 2024*; International Ground Source Heat Pump Association: Springfield, IL, USA, 2024; pp. 206–218.
68. Claprood, M.; Gloaguen, E.; Giroux, B.; Konstantinovskaya, E.; Malo, M.; Duchesne, M.J. Workflow using sparse vintage data for building a first geological and reservoir model for CO_2 geological storage in deep saline aquifer. *Greenh. Gases Sci. Technol.* **2012**, *2*, 260–278. [CrossRef]
69. Konstantinovskaya, E.; Rutqvist, J.; Malo, M. CO_2 storage and potential fault instability in the St. Lawrence Lowlands sedimentary basin (Quebec, Canada): Insights from coupled reservoir-geomechanical modeling. *Int. J. Greenh. Gas Control* **2014**, *22*, 88–110. [CrossRef]

70. Tran Ngoc, T.D.; Konstantinovskaya, E.; Lefebvre, R.; Malo, M. *Caractérisation Hydrogéologique et Pétrophysique des Aquifères Salins Profonds de la Région de Bécancour pour leur Potentiel de Séquestration Géologique du CO_2*; INRS: Québec, QC, Canada, 2011; Volume R-1318, 65p.
71. Chen, W.; Zhou, C.; Huang, X.; Luo, H.; Luo, Y.; Cheng, N.; Tian, Z.; Zhang, S.; Fan, J.; Zhang, L. Study on thermal radius and capacity of multiple deep borehole heat exchangers: Analytical solution, algorithm and application based on Response Factor Matrix method (RFM). *Energy* **2024**, *296*, 131132. [CrossRef]
72. Luo, Y.; Cheng, N.; Xu, G. Analytical modeling and thermal analysis of deep coaxial borehole heat exchanger with stratified-seepage-segmented finite line source method (S3-FLS). *Energy Build.* **2022**, *257*, 111795. [CrossRef]
73. Beier, R.A.; Morchio, S.; Fossa, M. Thermal response tests on deep boreholes through multiple ground layers. *Geothermics* **2022**, *101*, 102371. [CrossRef]
74. Schröder, E.; Thomauske, K.; Schmalzbauer, J.; Herberger, S.; Gebert, C.; Velevska, M. Design and test of a new flow calorimeter for online detection of geothermal water heat capacity. *Geothermics* **2015**, *53*, 202–212. [CrossRef]
75. Smith-Magowan, D.; Wood, R.H. Heat capacity of aqueous sodium chloride from 320 to 600 K measured with a new flow calorimeter. *J. Chem. Thermodyn.* **1981**, *13*, 1047–1073. [CrossRef]
76. VDI-Wärmeatlas. *VDI-Gesellschaft Verfahrenstechnik und Chemieingenieurwesen (GVC)*, 10th ed.; VDI-Verlag: Düsseldorf, Germany, 2006.
77. Chen, C.; Cai, W.; Naumov, D.; Tu, K.; Zhou, H.; Zhang, Y.; Kolditz, O.; Shao, H. Numerical investigation on the capacity and efficiency of a deep enhanced U-tube borehole heat exchanger system for building heating. *Renew. Energy* **2021**, *169*, 557–572. [CrossRef]
78. Brown, C.S.; Cassidy, N.J.; Egan, S.S.; Griffiths, D. A sensitivity analysis of a single extraction well from deep geothermal aquifers in the Cheshire Basin, UK. *Q. J. Eng. Geol. Hydrogeol.* **2022**, *55*, qjegh2021-2131. [CrossRef]
79. Ricard, L.P.; Sheldon, H.A.; Huddlestone-Holmes, C. Reservoir quality requirements for geothermal developments in deep sedimentary basin. In Proceedings of the World Geothermal Congress, Melbourne, Australia, 19–25 April 2015.
80. Van Wees, J.D.; Kronimus, A.; Van Putten, M.; Pluymaekers, M.; Mijnlieff, H.; Van Hooff, P.; Obdam, A.; Kramers, L. Geothermal aquifer performance assessment for direct heat production—Methodology and application to Rotliegend aquifers. *Neth. J. Geosci.* **2012**, *91*, 651–665. [CrossRef]
81. Phillips, S. *A Technical Databook for Geothermal Energy Utilization*; U.S. Department of Energy: Washington, DC, USA, 1981.
82. Adams, J.J.; Bachu, S. Equations of state for basin geofluids: Algorithm review and intercomparison for brines. *Geofluids* **2002**, *2*, 257–271. [CrossRef]
83. Perrochet, P. (GEOLEP, EPFL, Lausanne, Switzerland). Personal communication, 1996.
84. Diersch, H.J.; Kolditz, O. Coupled groundwater flow and transport: 2. Thermohaline and 3D convection systems. *Adv. Water Resour.* **1998**, *21*, 401–425. [CrossRef]
85. Diersch, H.J.G.; Bauer, D.; Heidemann, W.; Rühaak, W.; Schatzl, P. *Finite Element Formulation for Borehole Heat Exchangers in Modelling Geothermal Heating Systems by FEFLOW*; Wasy GmbH: Berlin, Germany; Institute of Thermodynamics and Thermal Engineering (ITW), University of Stuttgart: Stuttgart, Germany, 2010; 108p.

Disclaimer/Publisher's Note: The statements, opinions and data contained in all publications are solely those of the individual author(s) and contributor(s) and not of MDPI and/or the editor(s). MDPI and/or the editor(s) disclaim responsibility for any injury to people or property resulting from any ideas, methods, instructions or products referred to in the content.